HHS Public Access

Author manuscript

Cell Rep. Author manuscript; available in PMC 2021 September 23.

Published in final edited form as:

Cell Rep. 2020 February 11; 30(6): 1823–1834.e5. doi:10.1016/j.celrep.2020.01.042.

A FLCN-TFE3 Feedback Loop Prevents Excessive Glycogenesis and Phagocyte Activation by Regulating Lysosome Activity

Mitsuhiro Endoh[1,2,3,8,9,*], **Masaya Baba**[2,6,8,*], **Tamie Endoh**[1,2,3], **Akiyoshi Hirayama**[4], **Ayako Nakamura-Ishizu**[1,2], **Terumasa Umemoto**[2], **Michihiro Hashimoto**[2], **Kunio Nagashima**[5], **Tomoyoshi Soga**[4], **Martin Lang**[6], **Laura S. Schmidt**[6,7], **W. Marston Linehan**[6], **Toshio Suda**[1,2,*]

[1]Cancer Science Institute of Singapore, National University of Singapore, Centre for Translational Medicine, Singapore 117599, Singapore

[2]International Research Center for Medical Sciences (IRCMS), Kumamoto University, 2-2-1 Honjo, Chuo-ku, Kumamoto 860-0811, Japan

[3]Institute of Molecular Embryology and Genetics (IMEG), Kumamoto University, 2-2-1 Honjo, Chuo-ku, Kumamoto 860-0811, Japan

[4]Institute for Advanced Biosciences, Keio University, Tsuruoka, Yamagata 997-0052, Japan

[5]Leidos Biomedical Research, Inc., Frederick National Laboratory for Cancer Research, Frederick, MD, USA

[6]Urologic Oncology Branch, Center for Cancer Research, National Cancer Institute, Bethesda, MD 20892, USA

[7]Basic Science Program, Frederick National Laboratory for Cancer Research sponsored by the National Cancer Institute, Frederick, MD 21702, USA

[8]These authors contributed equally

[9]Lead Contact

SUMMARY

The tumor suppressor folliculin (FLCN) suppresses nuclear translocation of TFE3, a master transcription factor for lysosomal biogenesis, via regulation of amino-acid-sensing Rag GTPases. However, the importance of this lysosomal regulation in mammalian physiology remains unclear. Following hematopoietic-lineage-specific *Flcn* deletion in mice, we found expansion of vacuolated

[*]Correspondence: mendoh@kumamoto-u.ac.jp (M.E.), babam@kumamoto-u.ac.jp (M.B.), csits@nus.edu.sg (T.S.).

AUTHOR CONTRIBUTIONS

M.E., M.B., and T. Suda conceived the project. M.E., M.B., and T.E. designed and performed most experiments with input from L.S.S., W.M.L., and T. Suda. T.U. and M.H. performed fluorescence-activated cell sorting (FACS) analysis of hematopoietic lineage cells and participated in discussions of results. A.N.I. and K.N. performed and interpreted electron microscopy experiments. A.H. and T. Soga performed and interpreted metabolomics experiments. M.L. performed PAS staining of kidney sections from BHD patients. M.E. wrote the manuscript, which was edited by M.B., L.S.S., W.M.L., and T. Suda, with help from other authors.

DECLARATION OF INTERESTS

The authors declare no competing interests.

SUPPLEMENTAL INFORMATION

Supplemental Information can be found online at https://doi.org/10.1016/j.celrep.2020.01.042.

phagocytes that accumulate glycogen in their cytoplasm, phenotypes reminiscent of lysosomal storage disorder (LSD). We report that TFE3 acts in a feedback loop to transcriptionally activate FLCN expression, and FLCN loss disrupts this loop, augmenting TFE3 activity. *Tfe3* deletion in *Flcn* knockout mice reduces the number of phagocytes and ameliorates LSD-like phenotypes. We further reveal that TFE3 stimulates glycogenesis by promoting the expression of glycogenesis genes, including *Gys1* and *Gyg*, upon loss of *Flcn*. Taken together, we propose that the FLCN-TFE3 feedback loop acts as a rheostat to control lysosome activity and prevents excessive glycogenesis and LSD-like phagocyte activation.

INTRODUCTION

Appropriate cellular adaptation to nutrient availability is crucial for the maintenance of energy homeostasis at the cellular, tissue, and whole-body levels that when disrupted leads to diseases such as cancer (Cantor and Sabatini, 2012). Recent evidence indicates the importance of the lysosome in cellular energy metabolism not only by degrading self-proteins and organelles to recycle as a source of energy but also by sensing nutrient availability and regulating a cellular response to balance anabolic and catabolic processes (Lim and Zoncu, 2016; Saftig and Haas, 2016). Two main mediators of such lysosomal adaptation responses are the mTORC1 kinase complex and the MiTF/TFE family of transcription factors (MITF, TFEB, TFE3, and TFEC). These two factors are linked in a lysosome-to-nucleus signaling pathway that confers cells with the ability to adapt to nutrient availability and control their growth and survival (Martina et al., 2014a).

Folliculin (FLCN), germline mutations in which cause BirtHogg-Dubé (BHD) syndrome characterized by benign skin tumors, lung and kidney cysts, and kidney cancer (Birt et al., 1977; Nickerson et al., 2002; Schmidt, 2013; Vocke et al., 2005; Zbar et al., 2002), has been suggested to be one of the central regulators of the lysosomal nutrient sensing machinery. FLCN acts as a guanine nucleotide exchange factor (GEF) or a GTPase-activating protein (GAP) for the Rag family GTPases converting them to their active forms, which signal amino acid sufficiency to mammalian target of rapamycin complex 1 (mTORC1) (Petit et al., 2013; Tsun et al., 2013). It remains controversial as to whether FLCN regulates mTORC1 positively or negatively (Baba et al., 2016; Betschinger et al., 2013; El-Houjeiri et al., 2019; Hartman et al., 2009; Hasumi et al., 2009; Hudon et al., 2010; van Slegtenhorst et al., 2007; Wada et al., 2016). On the other hand, FLCN-deficient cells consistently display nuclear translocation of TFE3 and TFEB, master regulators of lysosomal biogenesis (Baba et al., 2016; Betschinger et al., 2013; El-Houjeiri et al., 2019; Hong et al., 2010; Petit et al., 2013; Wada et al., 2016). The guanosine diphosphate (GDP)-bound active form of Rag C/D GTPases interacts with TFE3 and TFEB, recruiting them to lysosomes where they are phosphorylated by mTORC1 and sequestered in the cytoplasm, whereas inactive Rags fail to interact with TFE3/TFEB (Martina et al., 2014b; Martina and Puertollano, 2013; Villegas et al., 2019). Thus, the impact of FLCN loss on intracellular localization of TFE3/TFEB can be in part explained by the activity of FLCN toward the lysosomal Rag GTPases.

Heterozygous Flcn knockout (KO) mice display increased susceptibility to renal cysts and neoplasia that is reminiscent of human BHD tumors (Hartman et al., 2009; Hasumi et

al., 2009; Hudon et al., 2010), demonstrating that the *Flcn*-KO mouse model faithfully recapitulates human BHD. Meanwhile, conditional *Flcn*-KO mouse models have revealed a function for *Flcn* in maintenance/homeostasis of a number of tissue and cell types such as kidney (Baba et al., 2008; Chen et al., 2008; Hasumi et al., 2009), lung (Goncharova et al., 2014), skeletal muscle (Hasumi et al., 2012), heart (Hasumi et al., 2014), adipocytes (Wada et al., 2016; Yan et al., 2016), B cells (Baba et al., 2012), hematopoietic stem cells (HSCs) (Baba et al., 2016), osteoclast cells (Baba et al., 2018), and monocytes/macrophages (Li et al., 2019), suggesting that FLCN has a fundamental role in the regulation/maintenance of diverse biological systems. However, it remains unclear whether and how chronic activation of TFE3 induces these specific phenotypes in tissue-specific *Flcn*-KO mice.

In this study, we aimed to elucidate the role of FLCN-mediated lysosomal regulation of cellular energy metabolism *in vivo*. Hematopoietic lineage-specific *Flcn*-KO mice show expansion of aberrantly vacuolated phagocytes that express gluconeogenesis genes and accumulate glycogen in their cytoplasm, phenotypes reminiscent of lysosomal storage disorder (LSD). We find that TFE3 acts in a feedback loop to transcriptionally activate FLCN expression, and FLCN loss disrupts this loop, augmenting TFE3 activity. *Tfe3* deletion in *Flcn*-KO mice reduces the number of phagocytes and ameliorates LSD-like phenotypes. We further reveal that TFE3 promotes the expression of glycogenesis genes, including *Gys1* and *Gyg*, upon loss of *Flcn*. Taken together, our study reveals a crucial role of the FLCN-TFE3 feedback loop in lysosomal control of glycogenesis and phagocyte activation that when disrupted leads to LSD-like phenotypes.

RESULTS

Flcn Depletion in Hematopoietic Lineages Induces Expansion of Abnormal Phagocytes

To assess a role of FLCN-mediated metabolic regulation in hema-topoiesis *in vivo*, we investigated $Flcn^{f/f}$; $Mx1\text{-}Cre^{Tg/+}$(*Flcn/Mx*-KO) mice, in which *Flcn* alleles are deleted following polyinosinic-poly-cytidylic acid (pIpC)-induced *Mx1*-Cre transgene expression (Schneider et al., 2003). *Flcn/Mx*-KO mice developed splenomegaly and hepatomegaly within 3 weeks of pIpC injection and died before 6 weeks (Figures S1A and S1B) (Baba et al., 2016). To precisely define effects of *Flcn* deletion in hematopoietic lineages and avoid potential pIpC-induced inflammatory responses, we generated $Flcn^{f/f}$; $Vav\text{-}iCre^{Tg/+}$(*Flcn/Vav*-KO) mice in which Cre recombinase is expressed under the control of the hematopoietic cell-specific Vav promoter. *Flcn/Vav*-KO mice were born at an aberrant Mendelian ratio (Figure 1A), survived no longer than 5 weeks (Figure 1B), and exhibited severe hepatosplenomegaly (Figure 1C), anemia, and thrombocytopenia (Figure 1D), phenocopying *Flcn/Mx*-KO mice. We conclude that hepatosplenomegaly seen in these mice is due to *Flcn* deficiency in hematopoietic cells. These phenotypes appear to be more severe than those of monocyte/macrophage-specific (Lyz-Cre) *Flcn*-KO mice (Li et al., 2019). To characterize the difference in bone marrow (BM) cell populations in *Flcn/Vav*-KO and control mice, we used mass cytometry by time-of-flight (CyTOF) to determine the expression of various hematopoietic cell lineage markers as well as intracellular signaling molecules. t-distributed stochastic neighbor embedding (t-SNE) analysis revealed an emergence of Mac-1^+ myeloid populations that exhibit abnormal upregulation of intracellular signaling pathways, including

β-catenin, HIF1A, AMPKα, STAT3, ERK, and AKT, in *Flcn/Vav*-KO BM cells (Figure 1E). Flow cytometry analysis further revealed expansion of Mac-1^+ $CD11c^+$ Ly-$6G^{mid}$ myeloid cells in BM, spleen, and liver of *Flcn/Vav*-KO mice (Figure 1F; liver data not shown). Giemsa staining of cytocentrifuge preparations of BM, spleen (Figure 1G), and liver (data not shown) demonstrated numerous large cytoplasm-rich myeloid cells, including some hemophagocytes, engulfing mature hematopoietic cells, such as erythrocytes and neutrophils, to varying degrees. We then employed a pHrodo *E. coli* BioParticles conjugate assay plus Mac-1 staining to confirm that most $Mac1^+$ cells in BM and SP of *Flcn/Vav*-KO mice exhibit marked internalization and acidification of the particles, which are activities indicative of phagocytic activity (Figure 1H). Taken together, these data demonstrate that *Flcn* depletion in hematopoietic lineages induces atypically activated Mac-1^+ $CD11c^+$ Ly-$6G^{mid}$ phagocytes in mice.

Flcn Depletion Stimulates Glycogenesis Pathway in Macrophages

To address the cell-autonomous effect of *Flcn* dysfunction in macrophages, we utilized the mouse macrophage cell line RAW 264.7 stably expressing a short hairpin RNA (shRNA) targeting *Flcn* (Figure S2A). We examined the phagocytic activity against pHrodo-succinimidyl ester (pHrodo-SE)-labeled whole BM cells from a wild-type mouse. *Flcn* knockdown (KD) in RAW cells marginally increased their phagocytic activity against untreated (i.e., mostly alive) BM cells (Figure 2A). In contrast, *Flcn*-KD RAW cells exhibited a marked increase in phagocytic activity against heat-treated BM cells (almost all cells are propidium iodide $[PI]^+$ Annexin V^+) compared to control RAW cells (Figures 2A and 2B), indicating loss of *Flcn* in macrophages cell-autonomously increases their phagocytic activity against dying/dead cells. These results suggest that *Flcn* depletion in macrophages stimulates phagocytic activity in a cell-autonomous manner, consistent with previous reports (El-Houjeiri et al., 2019; Li et al., 2019). To investigate FLCN-dependent metabolic regulation, we performed quantitative metabolomics analysis in murine monocyte/macrophage RAW 264.7 cells transduced with either control small interfering RNA (siRNA) or siRNA targeting *Flcn*, as we described previously (Baba et al., 2018). *Flcn* KD promoted a significant increase in intracellular levels of amino acids (Figure 2C), concordant with the fact that FLCN acts to convert the amino acid sensing Rag GTPases from an inactive to an active form that is necessary for mTORC1 activation on the lysosomal membrane (Tsun et al., 2013). *Flcn*-KD cells also showed markedly increased levels of UDPglucose, a precursor of glucose homopolymers such as glycogen, suggesting an effect on glycogen biosynthesis (Figure 2C). Quantitative RT-PCR analysis confirmed a significant upregulation of genes involving glycogenesis, including glycogen synthase 1 (*Gys1*) and glycogenin (*Gyg*), in *Flcn*-KD cells (Figure 2D). Taken together, these results suggest that *Flcn* depletion in macrophages stimulates the glycogen biosynthesis pathway in a cell-autonomous manner.

Hematopoietic-Lineage-Specific *Flcn* Deletion Induces Phagocytes Accumulating Cytoplasmic Glycogen Reminiscent of LSD

We then investigated glycogen synthesis in the phagocytes induced in *Flcn/Vav*-KO mice. Periodic acid-Schiff (PAS) staining of cytocentrifuge samples (Figure 3A) and paraffin sections (Figure 3B) demonstrated massive accumulation of PAS-positive substances in enlarged myeloid cells from BM, spleen and liver in *Flcn/Vav*-KO mice. Biochemical

analysis revealed significant increases in amounts of glycogen in *Flcn/Vav*-KO spleen tissues (Figure 3C). Quantitative RT-PCR analysis confirmed a significant upregulation of genes involving glycogenesis (*Gys1*, *Gyg*, and *Ppp1r3b*) in BM and spleen cells of *Flcn/Vav*-KO mice (Figure 3D). Moreover, quantitative RT-PCR analysis revealed abnormal upregulation of genes encoding the gluconeogenic enzymes fructose-1,6-bisphosphatase 1 (Fbp1) and glucose-6-phosphatase (G6pc) in BM and spleen cells of *Flcn/Vav*-KO mice (Figure 3E). These results suggest that hematopoietic-lineage-specific *Flcn* deletion in mice induces emergence of phagocytes accumulating cytoplasmic glycogen and that their infiltration of liver and spleen promotes hepatosplenomegaly reminiscent of LSD.

Loss of *Flcn* Upregulates Lysosomal Activity and Activates Tfe3 in Phagocytes

We next assessed potential mechanisms underlying LSD-like phenotypes in *Flcn*-KO mice. Transmission electron microscopy (TEM) analysis revealed that phagocytic myeloid cells seen in *Flcn*-KO mice exhibited numerous large vesicles, some of which appeared abnormal (multivesicular/multilamellar) (Figure 4A), suggesting augmentation of endosome/lysosome activity. We further found an increase in the mass of LysoTracker-sensitive acidic organelles (Figure 4B) and upregulated expression of lysosomal genes in BM (Figure 4C) and spleen cells (data not shown) in *Flcn*-KO mice. Consistently, expression levels of LAMP1 (a marker of late endosomes and lysosomes), GABARAP (an Atg8/LC3 family member implicated in autophagy), and TFE3 (a master transcription factor for lysosomal biogenesis and autophagy) were all markedly elevated (Figure 4D). Immunofluorescent staining of TFE3 on paraffin sections of spleen tissue (Figure 4E) and cytocentrifuge preparations of BM cells (Figure S3A) revealed a marked increase in expression and nuclear translocation of TFE3 in *Flcn/Vav*-KO mice, suggesting activation of TFE3 transcriptional activity. We also found increased nuclear TFE3 translocation following *Flcn* KD in murine monocyte/macrophage RAW 264.7 cells, indicating a cell-autonomous effect of *Flcn* loss on TFE3 activation (Figure S3B).

Enforced Expression of Nuclear TFE3 Activates Macrophages, in Part Recapitulating Myeloid Phenotypes Seen in *Flcn*-KO Mice

To determine to what extent TFE3 overexpression and nuclear translocation recapitulated phagocytic myeloid phenotypes observed in *Flcn/Vav*-KO mice, we expressed a transgene encoding TFE3 protein fused to the human glucocorticoid receptor ligand-binding domain (GR) in RAW cells and induced nuclear translocation of the fusion protein by dexamethasone (Dex) treatment, as described previously (Baba et al., 2016; Shimosato et al., 2007). Immunofluorescent staining with a TFE3 antibody showed Dex-treatment-dependent nuclear translocation of the TFE3-GR fusion protein (Figure 4F). Moreover, upon Dex treatment, those cells showed an increase in endosomal-lysosomal mass (Figure 4G) and marker expression (Figure 4H), as well as morphological changes reminiscent of activated macrophages (Figure 4I). We found increased expression of Mac-1 and CD11c (Figure 4J) and increased phagocytic activity following TFE3 activation (Figures 4K and S4A), similar to myeloid phenotypes seen in *Flcn/Vav*-KO mice (Figures 1F and 1H). We further verified that the TFE3-induced activation of macrophages was caused by upregulation of the lysosomal function using chloroquine, an inhibitor of lysosome acidification. The augmentation of phagocytic activity upon TFE3 activation by Dex treatment was mostly

cancelled by chloroquine treatment (Figure S4B). Therefore, these data indicate that the enforced expression of nuclear TFE3 activates macrophages and enhances their phagocytic activity through upregulation of lysosomal function.

TFE3 Acts in a Feedback Loop to Directly Activate *Flcn* Transcription

We next investigated Tfe3 function in *Flcn* expression. We found a significant increase in *Flcn* expression upon Tfe3 activation (Figure 5A) and, conversely, decreased *Flcn* expression following *Tfe3* KD in RAW cells (Figure 5B). Importantly, *Tfe3* KD further decreased *Flcn* transcript levels in *Flcn*-KD cells, suggesting that *Tfe3* partially rescues downregulated *Flcn* expression (Figure 5B). Moreover, we found a marked, *Tfe3*-dependent increase in levels of truncated *Flcn* transcripts in BM cells from *Flcn*-KO mice using primers specific for exons 3 and 4 (which can detect both full-length and truncated transcripts) (Figure 5C). By contrast, full-length *Flcn* transcripts (containing floxed exon 7) were undetectable under those conditions (Figure 5D) (see Figure 6E for primer positions). Analysis of TFE3 chromatin immunoprecipitation sequencing (ChIP-seq) data in a public database (Pastore et al., 2016) shows clear *Tfe3* binding at the *Flcn* transcription start site (TSS), where there is a known TFE3/TFEB-binding motif (TCACG) (Martina et al., 2014b; Palmieri et al., 2011), in nutrient-starved RAW cells (Figure 5E). Our ChIP-qPCR analysis also detected significant *Tfe3* enrichment at the *Flcn* TSS in wild-type BM cells, and those levels increased in BM cells from *Flcn/Vav*-KO mice (Figure 5F). We found *Tfe3*-dependent increases in levels of both trimethylated histone H3 lysine 4 (H3K4me3) and RNA polymerase II at the *Flcn* TSS in BM cells from *Flcn/Vav*-KO mice, which is indicative of increased transcription (Figure 5F). Taken together, these data support a model in which TFE3 acts in a feedback loop to directly activate *Flcn* transcription and suggest that *Flcn* loss perturbs this loop, facilitating TFE3 activation (Figure 5G).

Tfe3 Deletion in *Flcn*-KO Mice Ameliorates LSD-like Phenotypes

We next investigated whether and to what extent aberrantly activated TFE3 is responsible for LSD phenotypes seen in *Flcn/Vav*KO mice. *Tfe3* is located on the X chromosome. Thus, to generate mice lacking *Flcn* and either heterozygous or homozygous for *Tfe3*, we performed two crosses, one crossing $Flcn^{fl/+}$; $Vav\text{-}iCre^{Tg/+}$ male with female $Flcn^{f/f}$; $Tfe3^{-/+}$ mice and the other crossing $Flcn^{f/f}$ males with female $Flcn^{fl/+}$; $Vav\text{-}iCre^{Tg/+}$; $Tfe3^{-/+}$ mice. Those crosses combined yielded 145 total offspring of varying genotypes, of which 16 (11%) were either *Flcn/Vav*−KO/*Tfe3*null males ($Flcn^{fl/fl}$; $Vav\text{-}iCre^{tg/+}$; $Tfe3^{-/y}$) or *Flcn/Vav*−KO/*Tfe3* heterozygous females ($Flcn^{fl/fl}$; $Vav\text{-}iCre^{tg/+}$; $Tfe3^{-/+}$), reflecting overall the Mendelian model (12.5%). That ratio differed significantly from that of *Flcn/Vav*-KO mice harboring no *Tfe3*-KO allele (6 mice (4.1%)) (Figure S5A). Indeed, *Flcn/Vav*-KO mice harboring a *Tfe3*-KO allele grew to adulthood and survived >12 weeks (Figure 6A). While $Flcn^{fl/fl}$; $Vav\text{-}iCre^{tg/+}$; $Tfe3^{-/+}$ female mice exhibited obviously distended abdomens starting at ~2 months of age and died before 16 weeks of age, $Flcn^{fl/fl}$; $Vav\text{-}iCre^{tg/+}$; $Tfe3^{-/y}$ male mice (hereafter referred to as “dKO mice”) survived >16 weeks, demonstrating a *Tfe3*-allele-, dose-dependent rescue of survival in *Flcn/Vav*-KO mice (Figure 6A). Hepatosplenomegaly, anemia and thrombopenia phenotypes seen in *Flcn/Vav*-KO mice were significantly mitigated in dKO mice (Figures 6B and S5B). Flow cytometry analysis indicated a significant decrease in the Mac-1^{+} $CD11c^{+}$ Ly-$6G^{mid}$ histiocyte population but a significant

rescue of the Mac-1^+ Ly-$6G^{hi}$ mature neutrophil population in BM and spleen of dKO mice compared to *Flcn/Vav*-KO mice (Figure 6C; spleen data not shown). Giemsa staining of BM cells indicated a significant reduction in the frequency of hemophagocytosis in dKO mice compared to *Flcn/Vav*-KO mice (Figure 6D). Upregulation of LAMP-1 and lysosomal gene expression in BM cells in *Flcn/Vav*-KO mice was partially blocked in dKO mice, while *Tfe3* single-KO mice showed no apparent change in expression of these markers compared to wild-type mice (Figures 6E and 6F). Upregulation of the gluconeogenesis genes *Fbp1* and *G6pc* seen in *Flcn/Vav*-KO mice was also significantly blocked in dKO mice (Figures 6G and 6J). Accordingly, we found significant reduced glycogen levels in spleens of dKO mice compared to *Flcn/Vav*-KO mice (Figure 6H). Consistently, upregulation of the glycogenesis genes *Gys1*, *Gyg*, and *Ppp1r3b* was significantly blocked in dKO mice (Figures 6I and 6J). Phenotypes observed in *Flcn*/*Mx*-KO mice (such as poor survival, hepatosplenomegaly, and aberrant cell-surface profiling of myeloid cells) were also markedly rescued by simultaneous loss of *Tfe3* (Figure S6A–S6C). Taken together, these data demonstrate that *Tfe3* deficiency in*Flcn/Vav*-KO mice reduces the number of phagocytic histiocytes and mitigates hepatosplenomegaly, indicating that *Tfe3* activation promotes LSD-like phenotypes in FLCN-null settings. Finally, we investigated *Tfe3* function in the expression of glycogenesis genes. Analysis of TFE3 ChIP-seq data in a public database (Pastore et al., 2016) shows TFE3 binding at the TSSs of *Gys1* and *Gyg* in nutrient-starved RAW cells (Figure S7A). Our ChIP-qPCR analysis also detected significant TFE3 enrichment at the TSSs of *Gys1* and *Gyg* in BM cells from *Flcn/Vav*-KO mice (Figure 6K). These data indicate that TFE3 directly activates transcription of glycogenesis genes *Gys1* and *Gyg* upon *Flcn* loss.

Flcn Loss Stimulates Glycogenesis Flux via *Tfe3*

To examine the cell-autonomous role of the *Flcn*-*Tfe3* axis in glycogenesis and gluconeogenesis in macrophages, we utilized RAW 264.7 cells stably expressing either or both of *Flcn*- and *Tfe3*-targeting shRNA (Figure S2A and S2B). *Tfe3* deletion significantly blocked upregulation of *GYS1* and FBP1 expression upon *Flcn* deletion in RAW cells (Figure 7A). Accordingly, an increase in the level of UDP-glucose (an intermediate in glycogenesis) and fructose 1,6-bisphosphate (an intermediate in gluconeogenesis) seen in *Flcn*-KD cells (Figure 2C) was significantly blocked by additional KD of *Tfe3* (Figure 7B). To examine more directly whether the *Flcn*-*Tfe3* axis regulates glycogenesis and gluconeogenesis, we performed a ^{13}C-labeled pyruvate tracing assay. We analyzed ^{13}C-labeled intermediate metabolites in glycogenesis and gluconeogenesis pathways in RAW cells expressing either or both of *Flcn*- and *Tfe3*-targeting shRNA after addition of ^{13}C-labeled pyruvate to culture medium. Capillary electrophoresis–mass spectrometry (CE-MS) analysis revealed the presence of UDP-glucose and fructose 1,6-bisphosphate labeled with ^{13}C within 1 h after incubation with ^{13}C-labeled pyruvate (Figure 7C). *Flcn* KD increased the level of ^{13}C-labeled UDP-glucose and fructose 1,6-bisphosphate, and this increase was blocked by additional KD of *Tfe3* (Figure 7C). These data indicate that loss of *Flcn* stimulates glycogenesis and gluconeogenesis flux via *Tfe3* in myeloid cells.

DISCUSSION

The *Flcn*-*Tfe3* axis has been reported to be one of the critical regulators of cellular energy metabolism. Using hematopoietic-lineage-specific *Flcn*-KO mice, we demonstrate the following four findings: (1) *Flcn* KO induces expansion of aberrant phagocytes that accumulate glycogen in their cytoplasm, leading to hepatosplenomegaly reminiscent of LSD; (2) TFE3 acts in a feedback loop to transcriptionally activate FLCN expression, and FLCN loss disrupts the loop, increasing TFE3 activity; (3) *Tfe3* deletion in *Flcn*-KO mice reduces the number of histiocytes and ameliorates LSD-like phenotype; and (4) TFE3 stimulates glycogenesis by promoting the expression of glycogenesis genes, including *Gys1* and *Gyg*, upon loss of *Flcn*. Overall, the FLCN-TFE3 feedback loop acts as a rheostat to control lysosome activity and prevents excessive glycogenesis and LSD-like phagocyte activation.

Hepatosplenomegaly and phagocyte activation phenotypes observed in hematopoietic-lineage-specific *Flcn*-KO mice are reminiscent of LSD such as Niemann-Pick disease. However, phagocytes induced in the *Flcn*-KO mice are negative for Oil red O staining, suggesting no accumulation of lipid (data not shown). We instead found massive accumulation of glycogen in those phagocytes as determined by PAS staining and enzymatic assay. The primary tumor and cell line from FLCN-null BHD patients also exhibit intracellular glycogen accumulation (data not shown), consistent with a previous report (Possik et al., 2015). Taken together, the accumulation of intracellular glycogen is one of the common phenotypes observed in cells capable of surviving and proliferating in the absence of FLCN. Considering the role of FLCN in the regulation of Rag GTPase activity (Péli-Gulli et al., 2015; Petit et al., 2013; Tsun et al., 2013), those phenotypes appear to be in accord with a report demonstrating that KO of Rag GTPases in cardiomyocytes results in glycogen accumulation and phenocopies LSD (Kim et al., 2014). Thus, the glycogen storage phenotype might be caused by the absence of active forms of the Rag GTPases that activate mTORC1, leading to inactivation of TFE3/TFEB.

TFE3 has been shown to promote glycogen synthesis (Iwasaki et al., 2012; Izumida et al., 2013; Nakagawa et al., 2006), although the mechanism has been unclear. In this study, we elucidated a direct activation of glycogenesis genes *Gys1* and *Gyg* by TFE3 as an underlying mechanism for accumulation of glycogen upon FLCN loss. Since lysosomal acidification was not substantially impaired in FLCN-deficient phagocytes (pHrodo assay; Figures 2A and S4A), chronic activation of TFE3 in FLCN-deficient cells is not likely due to a decrease in lysosomal function but rather causes augmentation of lysosomal activities. Indeed, we found TFE3-dependent augmentation of both autophagosome and autolysosome formation in FLCNdeficient RAW cells and BHD renal cell carcinoma cells (data not shown), suggesting that loss of FLCN upregulates lysosomal functions, including autophagy, via activation of TFE3 irrespective of nutrient levels. It would be worth investigating in future studies whether the presence of excessive amino acids (Figure 2C) affects gluconeogenesis in FLCN-deficient phagocytes as well as in BHD kidney cancer cells.

STAR★METHODS

LEAD CONTACT AND MATERIALS AVAILABILITY

Further information and requests for resources and reagents should be directed to and will be fulfilled by the Lead Contact, Mitsuhiro Endoh (mendoh@kumamoto-u.ac.jp or mendoh0517@gmail.com). *Flcn* conditional KO mice used in this study are available with a completed Materials Transfer Agreement. All unique reagents generated in this study are available on request from the Lead Contact but we may require a completed Materials Transfer Agreement.

EXPERIMENTAL MODEL AND SUBJECT DETAILS

Mice—*Mx1-Cre*-driven *Flcn* conditional KO mice were described previously (Baba et al., 2016). *Vav-iCre* mice were obtained from the Jackson Laboratories (Bar Harbor, Maine, USA). *Tfe3* KO mice were obtained from Lino Tessarollo, Mouse Cancer Genetics Program, Frederick National Laboratory for Cancer Research, Frederick, MD USA. *Mx1-Cre*-mediated conditional knockout of *Flcn* was induced by three intraperitoneal doses of 20 mg/kg polyinosinic-polycytidylic acid (pIpC) (HMW; InvivoGen) every other day starting at 5–7 weeks of age. All mice were maintained on C57BL/6N background. For experiments, mice were randomly assigned to experimental groups, littermate-, age- and gender-matched; unless otherwise stated. Regarding the *Vav-iCre*-driven *Flcn* KO model, 3 to 4-week-old mice were used in each experiment. Regarding the *Mx1-Cre*-driven *Flcn* conditional KO model, 9 to 11-week-old mice (4 weeks after the first pIpC injection) were used in each experiment. All animal experiments were approved by Kumamoto University and carried out according to the guidelines of Kumamoto University for animal and recombinant DNA experiments. All animal work was also approved by the Institution of Animal Care and Use Committee (IACUC) and the Office of Safety, Health and Environment at the National University of Singapore.

RAW 264.7 Cell Lines—RAW 264.7 macrophage cell line cells were cultured in Dulbecco's modified Eagle medium (DMEM) (GIBCO) supplemented with 15% FCS, 100 U/ml penicillin, 100 μg/ml streptomycin. For generation of RAW cell clones stably expressing a TFE3-GR fusion protein, the expression construct (pCAG-Tfe3.GR-IRES-Puro) were transfected using Lipofectamine 2000 (Thermo Fisher Scientific) and stable transfectants were selected using 3.0 – 5.0 μg/mL puromycin (InvivoGen). To generate RAW cell clones stably expressing a scrambled (control) or a *Flcn*-specific shRNA, lentivirus particles produced using the modified pLVX-shRNA2-ZsGreen system (CMV promoter was replaced with PGK promoter) were infected and then ZsGreen-positive cells were single-cell sorted and expanded.

METHOD DETAILS

Flow Cytometry, Cell Sorting, and Analysis—Flow cytometric cell sorting was performed using Aria II (Becton Dickinson). Flow cytometry data were acquired on a LSR-II flow cytometer (Becton Dickinson) and analyzed using FlowJo software package (Tree Star). Fluorescent-dye-conjugated antibodies used were shown in the Key Resources Table.

Mass Cytometry Data Analysis—Mass Cytometry data of bone marrow cells from *Flcn/Vav*-KO and control mice were obtained using CyTOF2 (Fluidigm) according to the manufacturer's instructions and analyzed using Cytobank (https://www.cytobank.org/). Metal-conjugated antibodies used were shown in the Key Resources Table.

Immunocytochemistry—For detection of TFE3, cells were fixed with 4% paraformaldehyde in PBS for 10 min at room temperature, washed with PBS containing 0.3% Triton X-100, incubated with an antibody against either TFE3 (Sigma, #HPA023881) at 1:500 overnight at 4°C. Cells were washed in PBS, incubated with an Alexa Fluor-labeled anti-rabbit secondary antibody (Thermo Fisher Scientific) at 1:500 for 2 hours at room temperature, washed in PBS, and mounted with ProLong Gold antifade reagent with DAPI (Thermo Fisher Scientific). Fluorescence images were obtained using a confocal laser-scanning microscope (A1R, Nikon). Scanning was performed in sequential laser emission mode to avoid scanning at other wavelengths.

Phagocytosis Assay—Phagocytic activities of mouse bone marrow / spleen cells and RAW cells were assayed using the pHrodo *E.coli* BioParticles conjugate assay (Green or Red; Thermo Fisher Scientific) according to the manufacturer's instructions. Briefly, the cells seeded in wells of 96-well a round bottom tissue culture plate were mixed with the sonicated pHrodo *E.coli* BioParticles conjugate in Opti-MEM (Thermo Fisher Scientific) and incubated at 37°C for 60–90 minutes. Subsequently, the cells were washed, treated with Fcblock (CD16/CD32; BD Biosciences), stained with a PECy7-labeled Mac-1 antibody on ice, and subjected to FACS analysis to determine the fluorescence emission from the pH-sensitive pHrodo dye uptaked into the cells.

Phagocytic activities of RAW cells toward dying/dead hematopoietic cells were analyzed using heat-treated (for 3minutes at 60°C) whole bone marrow cells (BMCs) from wild-type mice. Untreated or heat-treated BMCs were labeled with pHrodo Red-succinimidyl ester (pHrodo Red-SE; at a final concentration of 150 nM) (Thermo Fisher Scientific) for 30 minutes at room temperature in PBS. RAW cells were labeled with CFSE (Thermo Fisher Scientific; at a final concentration of 2.5 μM), if necessary. EGFP-expressing or CFSE-labeled RAW cells were mixed with pHrodo Red-labeled BMCs and incubated for 2 hours. After the incubation, cells were collected and subjected to FACS analysis to determine the pHrodo signals in EGFP- or CFSE-positive RAW cells.

LysoTracker Assay—To monitor endosome-lysosome mass, cells were stained for lysosomes by using a LysoTracker Deep Red probe (Thermo Fisher Scientific) according to the manufacturer's instructions. Briefly, cells were treated with LysoTracker at a final concentration of 1 μM for 30 minutes at 37°C. The cells were further treated with Fcblock and stained with a Mac-1 antibody labeled with a fluorescent dye on ice, if necessary. The fluorescent intensities of LysoTracker (and Mac-1) were measured by flow cytometry.

Electron Microscopy (EM)—EM analysis was performed as previously described (Nagashima et al., 2011). Briefly, cells were fixed in glutaraldehyde (2% v/v) cacodylate buffer (0.1M, pH 7.4) for 1hr, washed in cacodylate buffer, postfixation was done in osmium tetroxide (1% v/v) for 1hr. en bloc stain in 0.5% w/v uranyl acetate (0.5% v/v) in acetate

buffer (0.1M, pH 4.5) for 1hr. Cells were dehydrated in a series of ethanol solution (35%, 50%, 75%, 95%, and 100%), and washed in a pure epoxy resin 3 times after 100% ethanol, and then embedded in the resin. The resin was cured in an oven (55°C) for 48 hours. The cured resin blocks were separated from the plate by submerging in liquid nitrogen. The cells were examined under an inverted microscope and areas were selected for thin-sections. 80 to 90nm thin sections were made and mounted on 200 copper mesh grids and counter stained in uranyl acetate and lead citrate. The grids were carbon coated in a vacuum evaporator, examined, and imaged in the electron microscope operated at 80kv, and digital images were taken by a CCD camera.

Periodic Acid–Schiff (PAS) Staining—PAS staining was performed using a PAS stain kit (#15792, MUTO PURE CHEMICALS) per manufacturer's instruction.

Glycogen Measurement—The levels of glycogen in mouse spleens and UOK257 cells were determined using a Glycogen Colorimetric/Fluorometric Assay Kit (#K646, BioVision) and a microplate reader (Tecan) per manufacturer's instruction.

Gene Expression Analysis (Quantitative RT-PCR)—Total RNA was extracted using TRIZOL (Thermo Fisher Scientific) or ISOGEN (Nippon Gene) followed by purification of DNA-free RNA with the RNeasy kit (QIAGEN, RNA cleanup protocol). For subsequent RT-PCR analysis, cDNA libraries were reverse transcribed using the SuperScript IV VILO Master Mix (Thermo Fisher Scientific) with random primers following the manufacturer's instructions. Quantitative real-time PCR was performed using SYBR green master mix (Thermo Fisher Scientific; A25742). Data were collected and analyzed on a QuantStudio 3 (Thermo Fisher Scientific). A mouse Actb gene was used to normalize samples. See Table S1 for primer sequences.

shRNA Knockdown in RAW 264.7 Cells—shRNA lentiviral vectors targeting mouse *Flcn* (target sequence: GCTTCAAGTCTCTTCGACACAT) and *Tfe3* (target sequence: GCCTAACATCAAACGCGAGAT) were purchased from VectorBuilder (Santa Clara, CA). HEK293T cells were co-transfected with shRNA-encoding plasmids plus Delta VPR envelope and CMV VSV-G packaging plasmids using FuGENE6, as described (Tsun et al., 2013). Virus-containing supernatants were collected 48 hours later, filtered, and concentrated using Amicon Ultra-15 centrifugal filters (Millipore). Target cells were infected by adding concentrated supernatants and 24 hours later selected in either puromycin or blasticidin and analyzed on the 5^{th} to 7^{th} day after infection.

Chromatin Immunoprecipitation (ChIP) Analysis—ChIP and subsequent quantitative PCR analysis was performed as previously described (Endoh et al., 2017). See Table S1 for primer sequences.

^{13}C Labeled Pyruvate Tracing Assay and Metabolome Analysis—RAW 264.7 cells expressing either or both of *Flcn*- and *Tfe3*-tageting shRNA were cultured in no pyruvate DMEM (044–29765, Wako) supplemented with 10% FCS and 1 mM of ^{13}C fully labeled sodium pyruvate (Cambridge isotope laboratories Inc.) for 15, 30, or 60

minutes. Metabolite extraction, CE-MS-based metabolomic profiling and data analysis were performed as previously described (Baba et al., 2018).

Phagocytosis Assay—Phagocytic activities of mouse bone marrow/spleen cells and RAW cells were assayed using the pHrodo *E.coli* BioParticles conjugate assay (Green or Red; Thermo Fisher Scientific) according to the manufacturer's instructions. Briefly, cells seeded in wells of 96-well round bottom tissue culture plates were mixed with sonicated BioParticle conjugates in Opti-MEM (Thermo Fisher Scientific) and incubated at 37°C for 60–90 minutes. Cells were then washed, treated with Fcblock (CD16/CD32; BD Biosciences), stained with a PECy7-labeled Mac-1 antibody on ice, and subjected to FACS analysis to assay fluorescence emission from the pH-sensitive pHrodo dye taken up by cells.

QUANTIFICATION AND STATISTICAL ANALYSIS

Statistical details of experiments can be found in figure legends. Quantification was performed from at least three independent experiments, and data were presented as mean ± SD unless otherwise specified. The Student's t test was used to compare two sets of data. Survival curves were constructed using the Kaplan–Meier method, and the difference between the curves was evaluated by a log–rank test. The χ^2 (chi-square) test was used to examine whether the distribution of mouse genotypes corresponds to Mendelian ratio. t-SNE analysis of CyTOF data was performed using Cytobank.

DATA AND CODE AVAILABILITY

This study did not generate any unique datasets or code.

Supplementary Material

Refer to Web version on PubMed Central for supplementary material.

ACKNOWLEDGMENTS

This research is supported by the National Research Foundation of Singapore and the Singapore Ministry of Education under its Research Centres of Excellence initiative. T. Suda was supported by a Singapore Translational Research (STaR) Investigator Award from the National Research Foundation of Singapore (NMRC/STaR/019/2014 and NMRC/STaR/18 may-0004) and in part by JSPS KAKENHI Grant-in-Aid for Scientific Research (S) (grant 26221309). M.E. was supported by JSPS KAKENHI Grants-in-Aid for Scientific Research (C) (grants 19K06693 and 16K07372) from the Ministry of Education, Culture, Sports, Science and Technology [MEXT] of Japan. M.B. was supported in part by JSPS KAKENHI Grants-in-Aid for Scientific Research (S, grants 18H05284 and 26221309; B, grant 18H02938; and C, 18K09140), a Grant-in-Aid for Challenging Research (exploratory; grants 18K19619 and 18K19553), the Joint Usage/Research Center Program of the Advanced Medical Research Center, Yokohama City University (Yokohama, Japan), and the program of the Joint Usage/Research Center for Developmental Medicine, Institute of Molecular Embryology and Genetics, Kumamoto University (Kumamoto, Japan). This project was funded in part by federal funds from the Frederick National Laboratory for Cancer Research (NIH) under contract HHSN261200800001E (L.S.S.). The content of this publication does not necessarily reflect the views or policies of the Department of Health and Human Services, nor does mention of trade names, commercial products, or organizations imply endorsement by the US Government. This research was supported by the Intramural Research Program of the NIH, National Cancer Institute, Center for Cancer Research.

REFERENCES

Baba M, Furihata M, Hong SB, Tessarollo L, Haines DC, Southon E, Patel V, Igarashi P, Alvord WG, Leighty R, et al. (2008). Kidney-targeted Birt-Hogg-Dube gene inactivation in a mouse model:

Erk1/2 and Akt-mTOR activation, cell hyperproliferation, and polycystic kidneys. J. Natl. Cancer Inst. 100, 140–154. [PubMed: 18182616]

Baba M, Keller JR, Sun HW, Resch W, Kuchen S, Suh HC, Hasumi H, Hasumi Y, Kieffer-Kwon KR, Gonzalez CG, et al. (2012). The folliculin-FNIP1 pathway deleted in human Birt-Hogg-Dubé syndrome is required for murine B-cell development. Blood 120, 1254–1261. [PubMed: 22709692]

Baba M, Toyama H, Sun L, Takubo K, Suh HC, Hasumi H, Nakamura-Ishizu A, Hasumi Y, Klarmann KD, Nakagata N, et al. (2016). Loss of folliculin disrupts hematopoietic stem cell quiescence and homeostasis resulting in bone marrow failure. Stem Cells 34, 1068–1082. [PubMed: 27095138]

Baba M, Endoh M, Ma W, Toyama H, Hirayama A, Nishikawa K, Takubo K, Hano H, Hasumi H, Umemoto T, et al. (2018). Folliculin regulates osteoclastogenesis through metabolic regulation. J. Bone Miner. Res. 33, 1785–1798. [PubMed: 29893999]

Betschinger J, Nichols J, Dietmann S, Corrin PD, Paddison PJ, and Smith A. (2013). Exit from pluripotency is gated by intracellular redistribution of the bHLH transcription factor *Tfe3*. Cell153, 335–347. [PubMed: 23582324]

Birt AR, Hogg GR, and Dubé WJ (1977). Hereditary multiple fibrofolliculomas with trichodiscomas and acrochordons. Arch. Dermatol. 113, 1674–1677. [PubMed: 596896]

Cantor JR, and Sabatini DM (2012). Cancer cell metabolism: one hallmark, many faces. Cancer Discov. 2, 881–898. [PubMed: 23009760]

Chen J, Futami K, Petillo D, Peng J, Wang P, Knol J, Li Y, Khoo SK, Huang D, Qian CN, et al. (2008). Deficiency of FLCN in mouse kidney led to development of polycystic kidneys and renal neoplasia. PLoS ONE 3, e3581. [PubMed: 18974783]

Dull T, Zufferey R, Kelly M, Mandel RJ, Nguyen M, Trono D, and Naldini L. (1998). A third-generation lentivirus vector with a conditional packaging system. Journal of virology72, 8463–8471. [PubMed: 9765382]

El-Houjeiri L, Possik E, Vijayaraghavan T, Paquette M, Martina JA, Kazan JM, Ma EH, Jones R, Blanchette P, Puertollano R, et al. (2019). The transcription factors TFEB and TFE3 link the FLCN-AMPK signaling axis to innate immune response and pathogen resistance. Cell Rep. 26, 3613–3628.e3616. [PubMed: 30917316]

Endoh M, Endo TA, Shinga J, Hayashi K, Farcas A, Ma KW, Ito S, Sharif J, Endoh T, Onaga N, et al. (2017). PCGF6-PRC1 suppresses premature differentiation of mouse embryonic stem cells by regulating germ cell-related genes. eLife 6, e21064.

Goncharova EA, Goncharov DA, James ML, Atochina-Vasserman EN, Stepanova V, Hong SB, Li H, Gonzales L, Baba M, Linehan WM, et al. (2014). Folliculin controls lung alveolar enlargement and epithelial cell survival through E-cadherin, LKB1, and AMPK. Cell Rep. 7, 412–423. [PubMed: 24726356]

Hartman TR, Nicolas E, Klein-Szanto A, Al-Saleem T, Cash TP, Simon MC, and Henske EP (2009). The role of the Birt-Hogg-Dubé protein in mTOR activation and renal tumorigenesis. Oncogene 28, 1594–1604. [PubMed: 19234517]

Hasumi Y, Baba M, Ajima R, Hasumi H, Valera VA, Klein ME, Haines DC, Merino MJ, Hong SB, Yamaguchi TP, et al. (2009). Homozygous loss of BHD causes early embryonic lethality and kidney tumor development with activation of mTORC1 and mTORC2. Proc. Natl. Acad. Sci. USA 106, 18722–18727. [PubMed: 19850877]

Hasumi Y, Baba M, Hasumi H, Huang Y, Lang M, Reindorf R, Oh HB, Sciarretta S, Nagashima K, Haines DC, et al. (2014). Folliculin (Flcn) inactivation leads to murine cardiac hypertrophy through mTORC1 deregulation. Hum. Mol. Genet. 23, 5706–5719. [PubMed: 24908670]

Hasumi H, Baba M, Hasumi Y, Huang Y, Oh H, Hughes RM, Klein ME, Takikita S, Nagashima K, Schmidt LS, et al. (2012). Regulation of mitochondrial oxidative metabolism by tumor suppressor FLCN. J. Natl. Cancer Inst. 104, 1750–1764. [PubMed: 23150719]

Hong SB, Oh H, Valera VA, Baba M, Schmidt LS, and Linehan WM (2010). Inactivation of the FLCN tumor suppressor gene induces TFE3 transcriptional activity by increasing its nuclear localization. PLoS ONE 5, e15793.

Hudon V, Sabourin S, Dydensborg AB, Kottis V, Ghazi A, Paquet M, Crosby K, Pomerleau V, Uetani N, and Pause A. (2010). Renal tumour suppressor function of the Birt-Hogg-Dubé syndrome gene product folliculin. J. Med. Genet. 47, 182–189. [PubMed: 19843504]

Iwasaki H, Naka A, Iida KT, Nakagawa Y, Matsuzaka T, Ishii KA, Kobayashi K, Takahashi A, Yatoh S, Yahagi N, et al. (2012). TFE3 regulates muscle metabolic gene expression, increases glycogen stores, and enhances insulin sensitivity in mice. Am. J. Physiol. Endocrinol. Metab. 302, E896–E902. [PubMed: 22297304]

Izumida Y, Yahagi N, Takeuchi Y, Nishi M, Shikama A, Takarada A, Masuda Y, Kubota M, Matsuzaka T, Nakagawa Y, et al. (2013). Glycogen shortage during fasting triggers liver-brain-adipose neurocircuitry to facilitate fat utilization. Nat. Commun. 4, 2316. [PubMed: 23939267]

Kim YC, Park HW, Sciarretta S, Mo JS, Jewell JL, Russell RC, Wu X, Sadoshima J, and Guan KL (2014). Rag GTPases are cardioprotective by regulating lysosomal function. Nat. Commun. 5, 4241. [PubMed: 24980141]

Li J, Wada S, Weaver LK, Biswas C, Behrens EM, and Arany Z. (2019). Myeloid folliculin balances mTOR activation to maintain innate immunity homeostasis. JCI Insight5, 126939.

Lim CY, and Zoncu R. (2016). The lysosome as a command-and-control center for cellular metabolism. J. Cell Biol. 214, 653–664. [PubMed: 27621362]

Martina JA, and Puertollano R. (2013). Rag GTPases mediate amino acid-dependent recruitment of TFEB and MITF to lysosomes. J. Cell Biol. 200, 475–491. [PubMed: 23401004]

Martina JA, Diab HI, Li H, and Puertollano R. (2014a). Novel roles for the MiTF/TFE family of transcription factors in organelle biogenesis, nutrient sensing, and energy homeostasis. Cell. Mol. Life Sci. 71, 2483–2497. [PubMed: 24477476]

Martina JA, Diab HI, Lishu L, Jeong-A L, Patange S, Raben N, and Puertollano R. (2014b). The nutrient-responsive transcription factor TFE3 promotes autophagy, lysosomal biogenesis, and clearance of cellular debris. Sci. Signal. 7, ra9.

Nagashima K, Zheng J, Parmiter D, and Patri AK (2011). Biological tissue and cell culture specimen preparation for TEM nanoparticle characterization. Methods Mol. Biol. 697, 83–91. [PubMed: 21116956]

Nakagawa Y, Shimano H, Yoshikawa T, Ide T, Tamura M, Furusawa M, Yamamoto T, Inoue N, Matsuzaka T, Takahashi A, et al. (2006). TFE3 transcriptionally activates hepatic IRS-2, participates in insulin signaling and ameliorates diabetes. Nat. Med. 12, 107–113. [PubMed: 16327801]

Nickerson ML, Warren MB, Toro JR, Matrosova V, Glenn G, Turner ML, Duray P, Merino M, Choyke P, Pavlovich CP, et al. (2002). Mutations in a novel gene lead to kidney tumors, lung wall defects, and benign tumors of the hair follicle in patients with the Birt-Hogg-Dubé syndrome. Cancer Cell 2, 157–164. [PubMed: 12204536]

Palmieri M, Impey S, Kang H, di Ronza A, Pelz C, Sardiello M, and Ballabio A. (2011). Characterization of the CLEAR network reveals an integrated control of cellular clearance pathways. Hum. Mol. Genet. 20, 3852–3866. [PubMed: 21752829]

Pastore N, Brady OA, Diab HI, Martina JA, Sun L, Huynh T, Lim JA, Zare H, Raben N, Ballabio A, and Puertollano R. (2016). TFEB and TFE3 cooperate in the regulation of the innate immune response in activated macrophages. Autophagy12, 1240–1258. [PubMed: 27171064]

Péli-Gulli MP, Sardu A, Panchaud N, Raucci S, and De Virgilio C. (2015). Amino acids stimulate TORC1 through Lst4-Lst7, a GTPase-activating protein complex for the Rag family GTPase Gtr2. Cell Rep. 13, 1–7. [PubMed: 26387955]

Petit CS, Roczniak-Ferguson A, and Ferguson SM (2013). Recruitment of folliculin to lysosomes supports the amino acid-dependent activation of Rag GTPases. J. Cell Biol. 202, 1107–1122. [PubMed: 24081491]

Possik E, Ajisebutu A, Manteghi S, Gingras MC, Vijayaraghavan T, Flamand M, Coull B, Schmeisser K, Duchaine T, van Steensel M, et al. (2015). FLCN and AMPK confer resistance to hyperosmotic stress via remodeling of glycogen stores. PLoS Genet. 11, e1005520.

Saftig P, and Haas A. (2016). Turn up the lysosome. Nat. Cell Biol. 18, 1025–1027. [PubMed: 27684505]

Schmidt LS (2013). Birt-Hogg-Dubé syndrome: from gene discovery to molecularly targeted therapies. Fam. Cancer 12, 357–364. [PubMed: 23108783]

Schneider A, Zhang Y, Guan Y, Davis LS, and Breyer MD (2003). Differential, inducible gene targeting in renal epithelia, vascular endothelium, and viscera of Mx1Cre mice. Am. J. Physiol. Renal Physiol. 284, F411–F417. [PubMed: 12529277]

Shimosato D, Shiki M, and Niwa H. (2007). Extra-embryonic endoderm cells derived from ES cells induced by GATA factors acquire the character of XEN cells. BMC Dev. Biol. 7, 80. [PubMed: 17605826]

Tsun ZY, Bar-Peled L, Chantranupong L, Zoncu R, Wang T, Kim C, Spooner E, and Sabatini DM (2013). The folliculin tumor suppressor is a GAP for the RagC/D GTPases that signal amino acid levels to mTORC1. Mol. Cell 52, 495–505. [PubMed: 24095279]

van Slegtenhorst M, Khabibullin D, Hartman TR, Nicolas E, Kruger WD, and Henske EP (2007). The Birt-Hogg-Dube and tuberous sclerosis complex homologs have opposing roles in amino acid homeostasis in Schizosacchar-omyces pombe. J. Biol. Chem. 282, 24583–24590. [PubMed: 17556368]

Villegas F, Lehalle D, Mayer D, Rittirsch M, Stadler MB, Zinner M, Olivieri D, Vabres P, Duplomb-Jego L, De Bont E, et al. (2019).). Lysosomal signaling licenses embryonic stem cell differentiation via inactivation of Tfe3. Cell Stem Cell 24, 257–270.e8. [PubMed: 30595499]

Vocke CD, Yang Y, Pavlovich CP, Schmidt LS, Nickerson ML, Torres-Cabala CA, Merino MJ, Walther MM, Zbar B, and Linehan WM (2005). High frequency of somatic frameshift BHD gene mutations in Birt-Hogg-Dubé associated renal tumors. J. Natl. Cancer Inst. 97, 931–935. [PubMed: 15956655]

Wada S, Neinast M, Jang C, Ibrahim YH, Lee G, Babu A, Li J, Hoshino A, Rowe GC, Rhee J, et al. (2016). The tumor suppressor FLCN mediates an alternate mTOR pathway to regulate browning of adipose tissue. Genes Dev. 30, 2551–2564. [PubMed: 27913603]

Yan M, Audet-Walsh É, Manteghi S, Dufour CR, Walker B, Baba M, St-Pierre J, Giguère V, and Pause A. (2016). Chronic AMPK activation via loss of FLCN induces functional beige adipose tissue through PGC-1α/ERRα. Genes Dev. 30, 1034–1046. [PubMed: 27151976]

Zbar B, Alvord WG, Glenn G, Turner M, Pavlovich CP, Schmidt L, Walther M, Choyke P, Weirich G, Hewitt SM, et al. (2002). Risk of renal and colonic neoplasms and spontaneous pneumothorax in the Birt-HoggDubé syndrome. Cancer Epidemiol. Biomarkers Prev. 11, 393–400. [PubMed: 11927500]

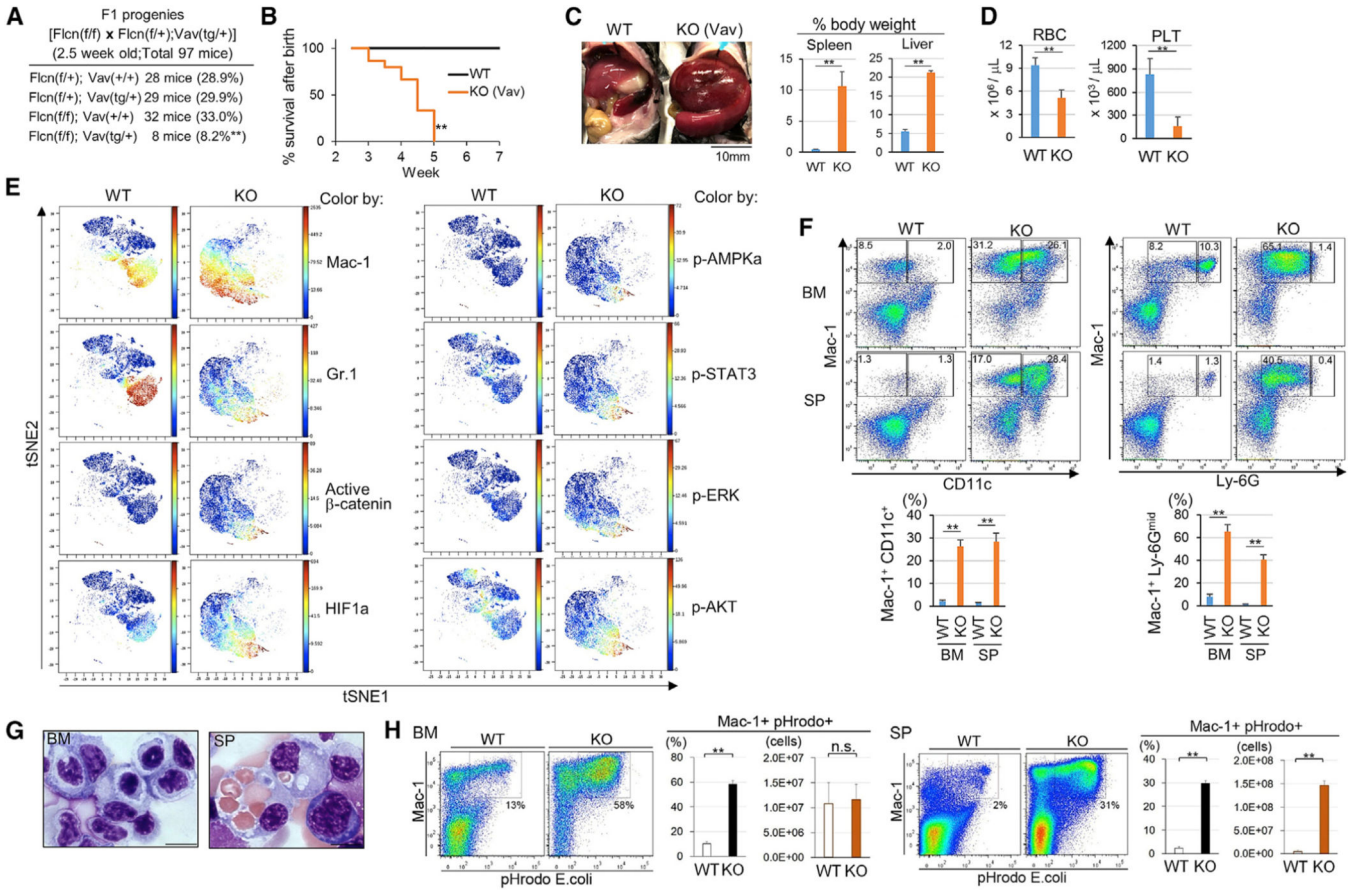

Figure 1. *Flcn* Depletion in Hematopoietic Lineages Induces Expansion of Abnormal Phagocytes

(A) Genotypes of progeny of crosses between $Flcn^{f/f}$ and $Flcn^{f/+}$; $Vav\text{-}iCre^{Tg/+}$ mice. **p ≤ 0.01 (χ^2 test).

(B) Kaplan-Meier survival analysis shows a statistically significant difference between $Flcn^{f/f}$ (wild type [WT]) and $Flcn^{f/f}$;$Vav\text{-}iCre^{Tg/+}$ (*Flcn/Vav*-KO) mice (log-rank test: **p ≤ 0.01).

(C) Gross images of spleens and livers of *Flcn/Vav*-KO and control mice at 4 weeks of age. Scale bar, 10 mm. Graphs represent mean percent spleen/body and liver/body weight of *Flcn/Vav*-KO and control mice at 4 weeks of age (mean ± SD; n = 4; **p ≤ 0.01 by Student's t test).

(D) Numbers of red blood cells (RBCs) and platelets (PLTs) in peripheral blood from *Flcn/Vav*-KO and control mice at 4 weeks of age (mean ± SD; n = 4; **p ≤ 0.01 by Student's t test).

(E) t-SNE plots showing the distribution of BM cells expressing various hematopoietic lineage markers and intracellular signaling molecules (see STAR Methods for details) obtained from *Flcn/Vav*-KO and control mice at 4 weeks of age. The intensity of staining with the indicated antibodies is shown in color graduation from red to yellow to blue (n = 3).

(F) Flow cytometry analysis demonstrating induction of $Mac1^{hi}$ $CD11c^{hi}$ $Ly\text{-}6G^{mid}$ large myeloid cells in BM and spleen of *Flcn/Vav*-KO mice. The numbers in plots represent percentage of the gated population. Graphs represent percentage of the indicated population (mean ± SD; n = 4; **p ≤ 0.01 by Student's t test).

(G) Giemsa staining of cytocentrifuged BM and spleen (SP) cells from *Flcn/Vav*-KO and control mice at 4 weeks of age. Scale bar, 10 μm.

(H) Phagocytosis assay using pHrodo *E. coli* BioParticle conjugates in combination with Mac-1 staining. Analysis reveals an increase in the proportion and number of Mac-1^+ phagocytic myeloid cells in BM and spleen cells of *Flcn/Vav*-KO mice. The numbers in plots represent percentage of the gated population. Graphs represent percentage and absolute number of the indicated population (mean ± SD; n = 4; **p ≤ 0.01 by Student's t test).

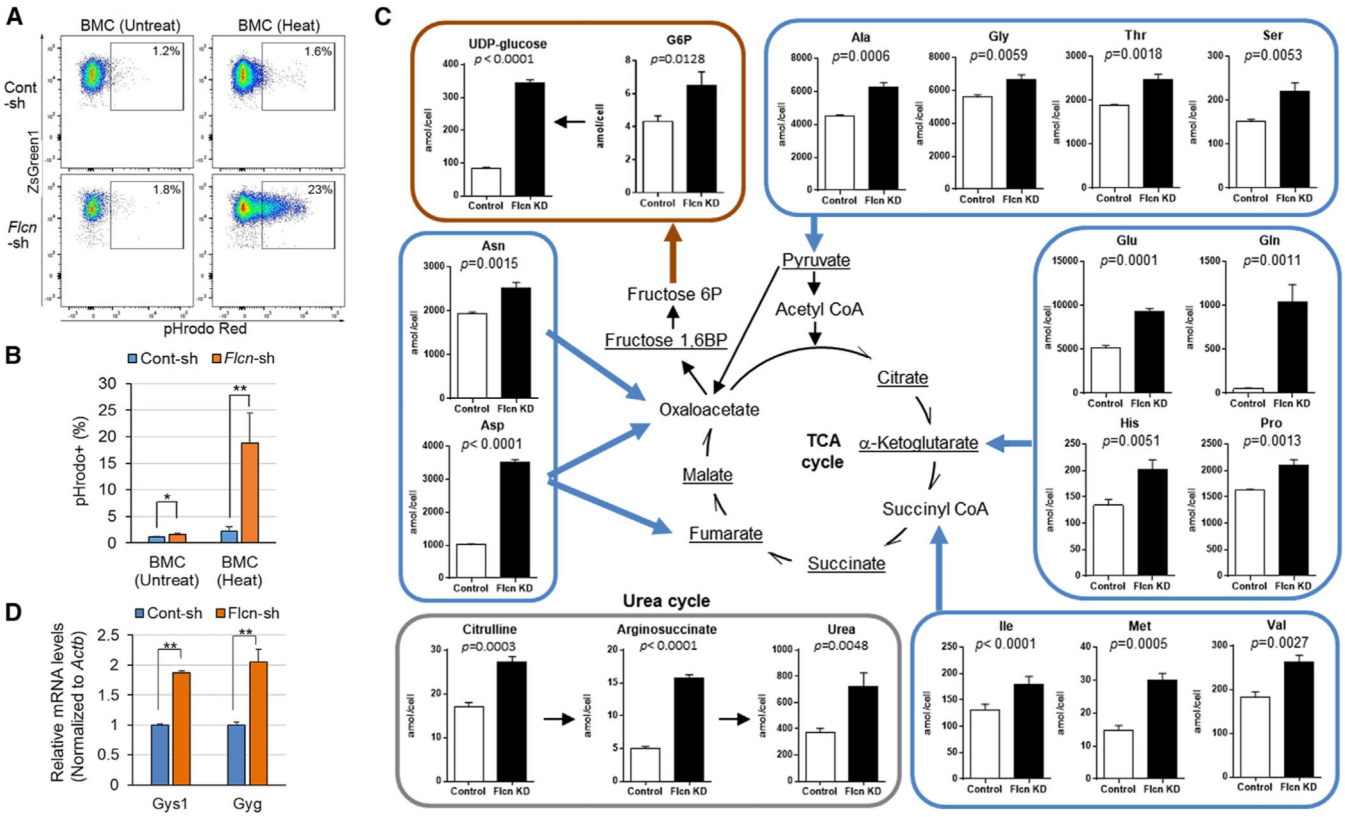

Figure 2. *Flcn* Depletion Cell-Autonomously Stimulates Glycogenesis Pathways in Macrophages

(A and B) Detection of phagocytic activity of RAW 264.7 cells expressing a control shRNA or an shRNA targeting *Flcn* against pHrodo-SE-labeled untreated or heat-treated (for 3 min at 60°C) bone marrow cells (BMC) by flow cytometry. Representative fluorescence-activated cell sorting (FACS) plots are shown (A). Mean fluorescence intensities (MFIs) of pHrodo red in ZsGreen1-positive RAW cells were analyzed and are graphically represented (B) (n = 4; *p < 0.05, **p < 0.01 by Student's t test).

(C) Upregulation of metabolites associated with glycogen biosynthesis by *Flcn* KD, as determined by capillary electrophoresis time-of-flight mass spectrometry (CE-TOF/MS) comprehensive metabolome analysis of siRNA-transfected Raw264.7 cells. y axis indicates amol/cell. Shown are means ± SD. Metabolites underlined in the pathway were significantly upregulated (p ≤ 0.01; n = 3). p values were calculated by unpaired t test.

(D) The mRNA expression of glycogenesis genes (*Gys1* and *Gyg*1) in RAW 264.7 cells expressing a control shRNA or an shRNA targeting *Flcn* was determined by quantitative RT-PCR and normalized to that of *Actb* (mean ± SD; n = 4; **p ≤ 0.01 by Student's t test).

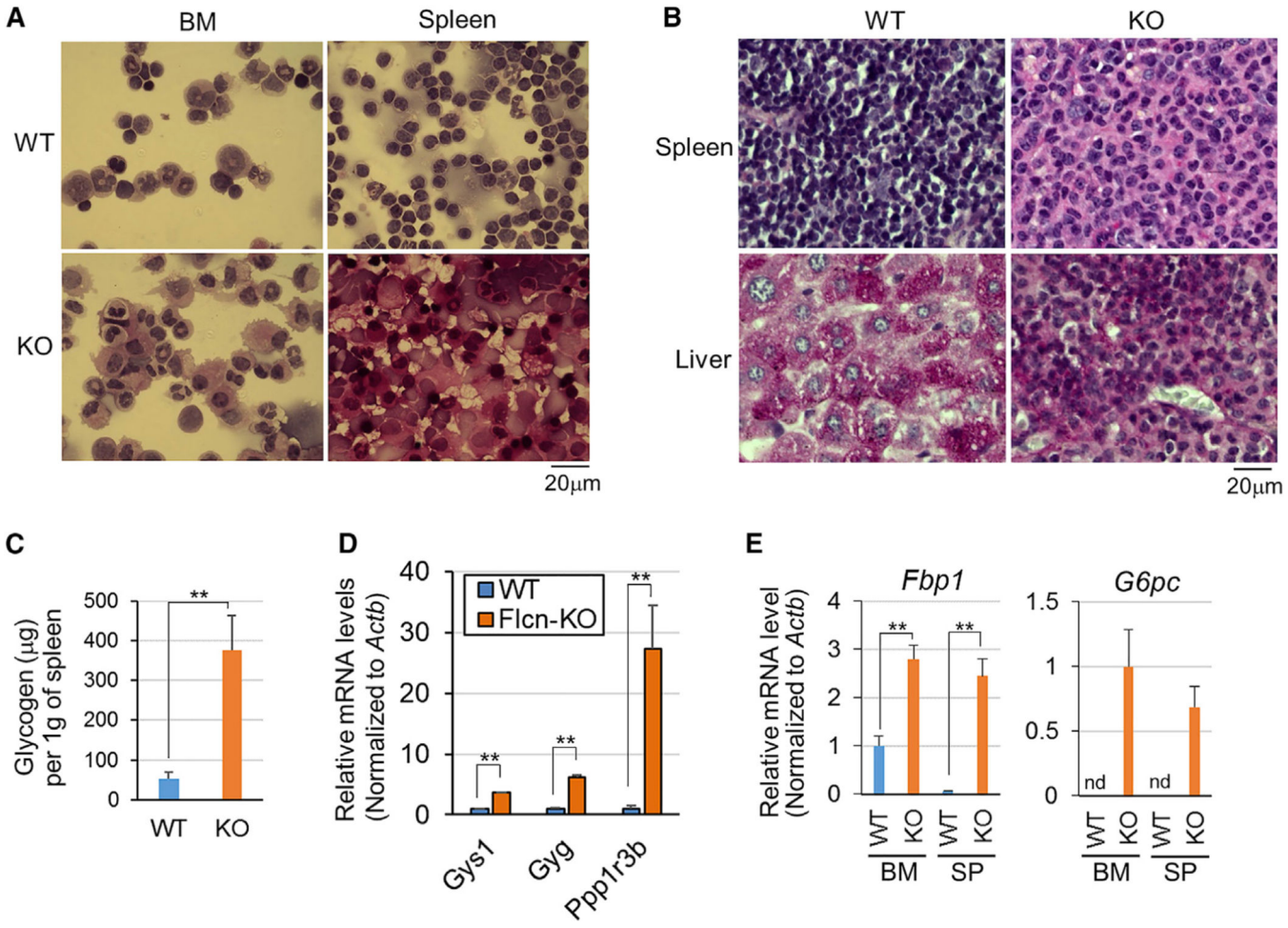

Figure 3. Hematopoietic-Lineage-Specific *Flcn* Deletion in Mice Induces Phagocytes Accumulating Cytoplasmic Glycogen, Reminiscent of Lysosomal Storage Disorder (LSD)

(A) Periodic acid-Schiff (PAS) staining of cytocentrifuged BM and spleen (SP) cells from *Flcn/Vav*-KO and control mice at 4 weeks of age. Scale bar, 20 μm.

(B) PAS staining of paraffin sections from spleens of *Flcn/Vav*-KO and control mice at 4 weeks of age. Scale bar, 20 μm.

(C) Biochemical measurement of glycogen levels in spleen tissues of *Flcn/Vav*-KO and control mice at 4 weeks of age. Glycogen levels were determined using an enzyme-based fluorometric assay kit (mean ± SD; n = 4; **p ≤ 0.01 by Student's t test).

(D) Expression of the glycogenesis genes *Gys1*, *Gyg*1, and *Ppp1r3b* in spleen cells from *Flcn/Vav*-KO and control mice at 4 weeks of age, as determined by quantitative RT-PCR. Data were normalized to *Actb* (mean ± SD; n = 4; **p ≤ 0.01 by Student's t test).

(E) Expression of the gluconeogenesis genes *Fbp1* and *G6pc* in BM and spleen cells from *Flcn/Vav*-KO and control mice at 4 weeks of age, as determined by quantitative RT-PCR. Data were normalized to Actb (mean ± SD; n = 4; nd, not detected; **p ≤ 0.01 by Student's t test).

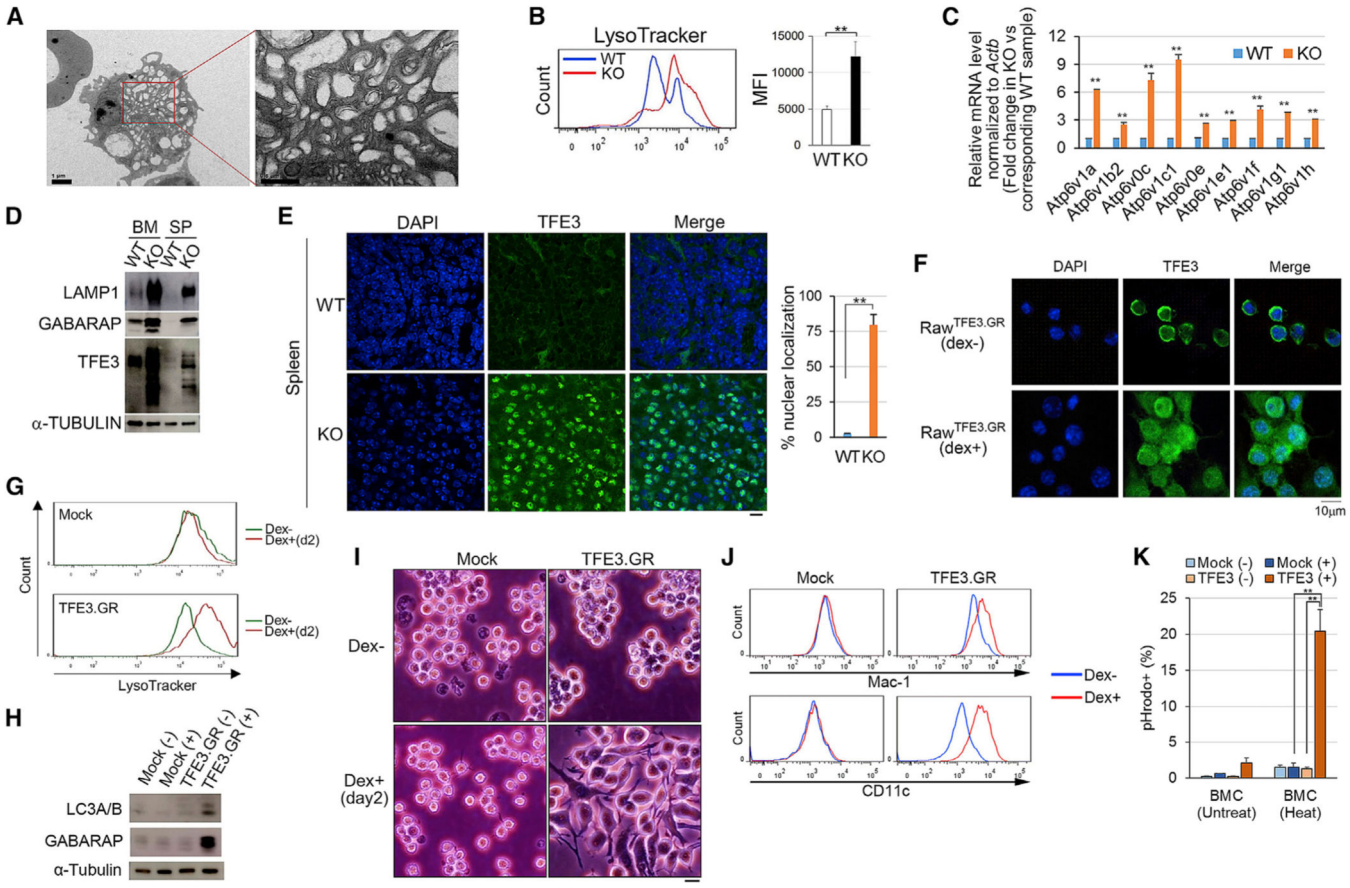

Figure 4. Loss of *Flcn* Upregulates Lysosomal Activity and Activates Tfe3 in Phagocytes

(A) Transmission electron microscopy (TEM) images showing numerous endosome-lysosome structures in Mac1^{+} myeloid cells collected from BM of *Flcn/Vav*-KO mice. Right: higher magnification of the square in left image. Scale bars represent 1 μm (upper panel) and 0.5 μm (lower panel).

(B) LysoTracker staining demonstrating an increase in acidic endosome-lysosome mass in whole BM cells from *Flcn/Vav*-KO compared to control mice (mean ± SD; n = 4; **p ≤ 0.01 by Student's t test).

(C) Quantitative RT-PCR results showing expression of indicated lysosomal genes in BM cells from *Flcn/Vav*-KO mice. Data were normalized to *Actb*. For each transcript tested, WT values were arbitrarily set to 1 and fold-changes calculated in KO samples (mean ± SD; n = 4; *p ≤ 0.05, **p ≤ 0.01 by Student's t test).

(D) Western blot showing upregulation of LAMP1 (a lysosome marker), GABARAP (an autophagy marker), and TFE3 (a master regulator of lysosome biogenesis and autophagy) in BM and SP cells of *Flcn/Vav*-KO mice.

(E) Immunofluorescence staining for TFE3 (green) demonstrates TFE3 nuclear translocation in splenocytes from *Flcn/Vav*-KO mice. Nuclei were counterstained with DAPI (blue). Scale bar, 10 μm. Graph represents the percentage of cells showing nuclear TFE3 staining among all cell nuclei in splenocytes from *Flcn/Vav*-KO and control mice (mean ± SD; n = 3; **p ≤ 0.01 by Student's t test).

(F) Significantly increased nuclear TFE3 (green) immunostaining as seen in RAW cells expressing a TFE3-GR construct and cultured with (+) dexamethasone (Dex;100 nM) for 1 day. Predominantly cytoplasmic TFE3 staining (green) was seen in cells cultured without (−) Dex. Nuclei were counterstained with DAPI (blue). Scale bar, 10 μm.

(G) Flow cytometry analysis of LysoTracker-stained RAW cells expressing either a control or TFE3-GR construct cultured with (+) or without (−) Dex for 2 days revealed a significant increase in lysosomal mass by the overexpression of nuclear TFE3.

(H) TFE3 activation increases expression of GABARAP proteins. Western blotting with anti-LC3A/B and anti-GABARAP antibodies was performed using whole-cell lysates from RAW cells stably expressing a mock or TFE3-GR construct and cultured with (+) or without (−) Dex for 2 days.

(I) Phase-contrast image showing that RAW cells stably expressing the TFE3-GR construct undergo marked changes in cell morphology after 2 days of Dex treatment. Scale bar, 10 μm.

(J) Representative flow cytometry analysis showing changes in expression of Mac-1 and CD11c in RAW cells stably expressing a mock or TFE3-GR construct and either untreated (−; blue line) or treated (+; red line) with Dex for 2 days, recapitulating histiocyte phenotypes seen in *Flcn*-KO mice.

(K) Phagocytic assay using pHrodo *E. coli* BioParticles conjugate. Subsequent FACS analysis shows marked increases in phagocytic activity in RAW cells expressing a TFE3-GR construct, but not in those expressing a mock construct, after Dex treatment for 2 days. Bars in the graph represent mean ± SD fluorescence intensities of pHrodo red ($n = 4$; $^{**}p \leq 0.01$ by Student's t test).

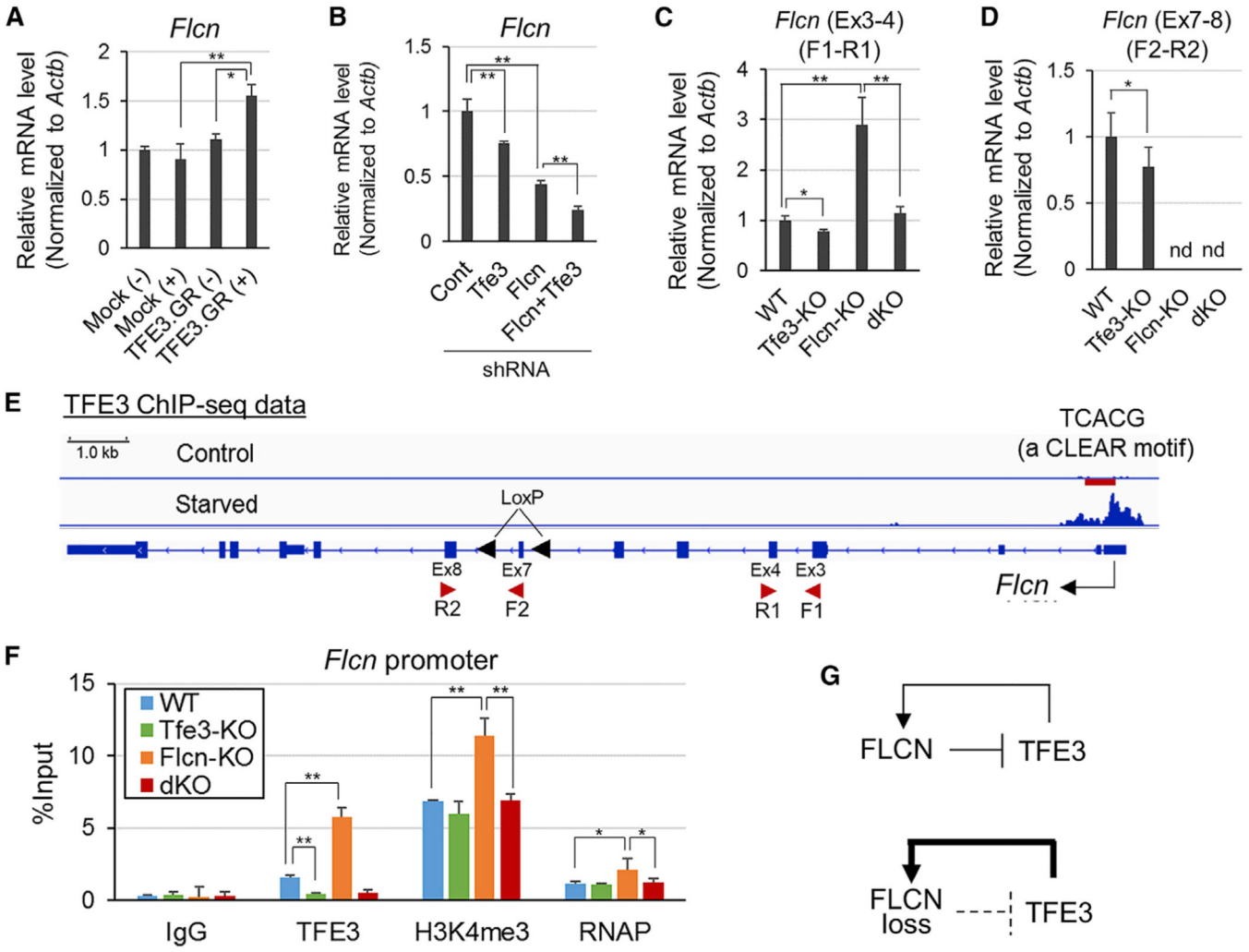

Figure 5. TFE3 Acts in a Feedback Loop to Directly Activate *Flcn* Transcription

(A) *Flcn* transcript levels in RAW cells expressing either a control or TFE3-GR construct and cultured with (+) or without (−) Dex for 2 days were determined by quantitative RT-PCR and normalized to *Actb* levels. Bars represent fold-change of values relative to Dex-untreated control cells (mean ± SD; *p ≤ 0.05, **p ≤ 0.01 by Student's t test).

(B) *Flcn* transcript levels in RAW cells expressing indicated shRNA as determined in (A).

(C and D) Levels of *Flcn* transcripts containing floxed exon 7 (D); detected by primers specific for full-length transcripts) or exons 3–4 (C); detected by primers capable of amplifying both intact and truncated transcripts) in BM cells from $Flcn^{f/f}$ (WT), $Tfe3^{-/y}$ (*Tfe3*-KO), $Flcn^{f/f}$;$Vav\text{-}iCre^{Tg/+}$ (*Flcn*-KO), or $Flcn^{f/f}$;$Vav\text{-}iCre^{Tg/+}$; $Tfe3^{-/y}$ (dKO) mice were determined as in (A) using primers shown in (E) (mean ± SD; nd, not detected; *p ≤ 0.05, **p ≤ 0.01 by Student's t test).

(E) TFE3 ChIP-seq data (SRX1471834 and SRX1471835) demonstrate TFE3 binding to the *Flcn* transcription start site (TSS), which contains a TFEB/TFE3-binding motif (TCAGC) (Martina et al., 2014b; Palmieri et al., 2011), in nutrient-starved RAW cells. Filled red triangles indicate positions of loxP sites in the floxed *Flcn* allele. Positions of primer sets used in (C) and (D) are also shown.

(F) ChIP-qPCR analysis of levels of TFE3, trimethylated histone H3 lysine 4 modification (H3K4me3), and RNA polymerase II at the *Flcn* TSS in BM cells from $Flcn^{f/f}$ (WT), $Tfe3^{-/y}$ (*Tfe3*-KO), $Flcn^{f/f}$;$Vav\text{-}iCre^{Tg/+}$ (*Flcn*-KO), or $Flcn^{f/f}$;$Vav\text{-}iCre^{Tg/+}$;$Tfe3^{-/y}$ (dKO) mice. Relative amounts of ChIPed DNA are depicted as a percentage of input DNA (mean ± SD; n = 4; *p ≤ 0.05, **p ≤ 0.01 by Student's t test).

(G) Schematic showing the FLCN-TFE3 feedback.

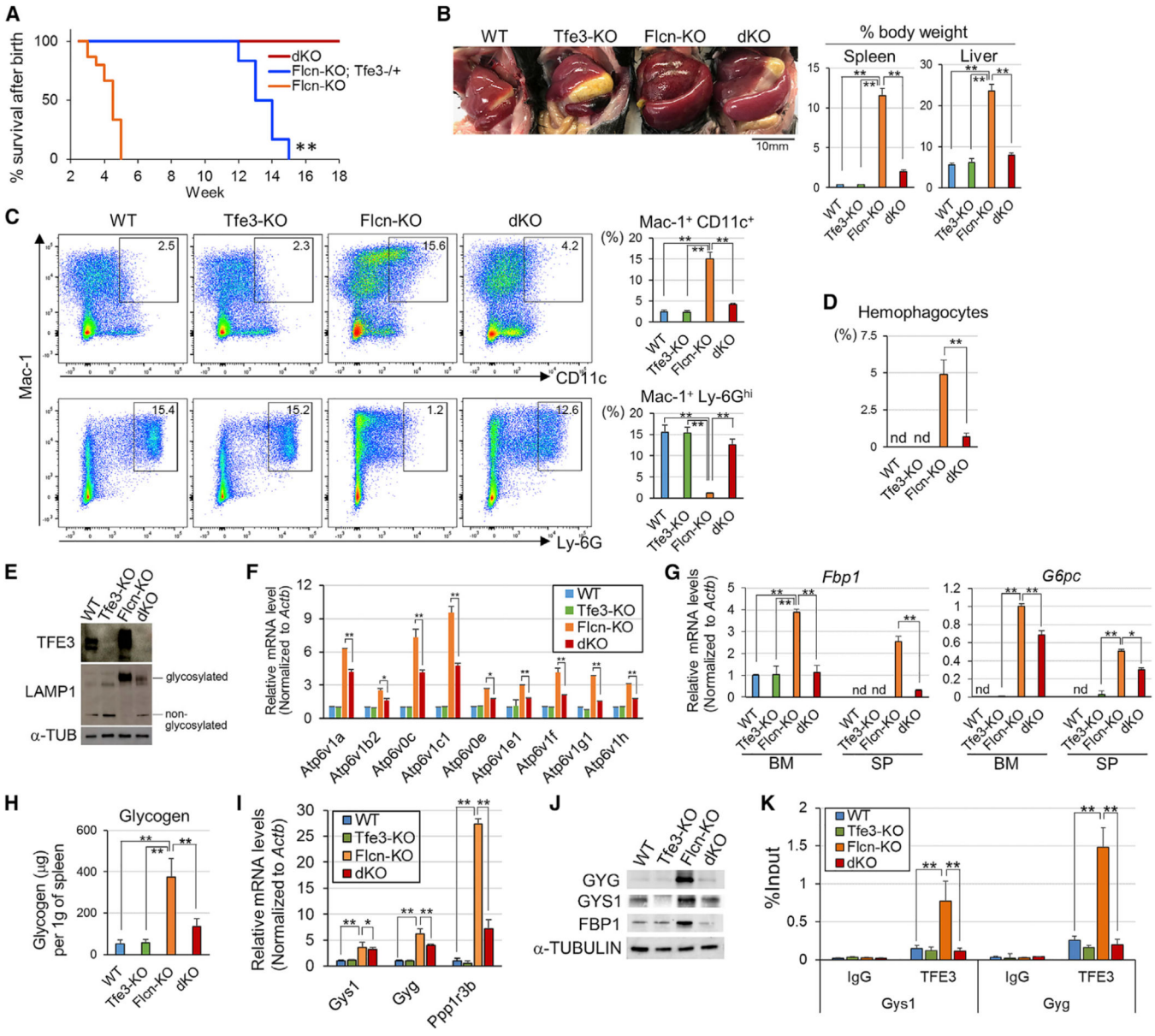

Figure 6. *Tfe3* Deletion in *Flcn*-KO Mice Ameliorates LSD-like Phenotypes

(A) Kaplan-Meier survival analysis demonstrating *Tfe3* allele dose-dependent rescue of *Flcn*$^{f/f}$;*Vav-iCre*$^{Tg/+}$ (*Flcn*-KO) mouse survival. *Flcn*$^{f/f}$;*Vav-iCre*$^{Tg/+}$;*Tfe3*$^{-/+}$ (female) mice are indicated as "*Flcn*-KO;*Tfe3*$^{-/+}$". *Flcn*$^{f/f}$;*Vav-iCre*$^{Tg/+}$;*Tfe3*$^{-/y}$ (male) and *Flcn*$^{f/f}$;*Vav-iCre*$^{Tg/+}$;*Tfe3*$^{-/-}$ (female) mice are indicated as "dKO" (**p ≤ 0.01, log-rank test). See Figure S5A for more details.

(B) Gross images of spleens and livers of *Flcn*$^{f/f}$ (WT), *Tfe3*$^{-/y}$ (*Tfe3*-KO), *Flcn*$^{f/f}$;*Vav-iCre*$^{Tg/+}$ (*Flcn*-KO), and *Flcn*$^{f/f}$;*Vav-iCre*$^{Tg/+}$;*Tfe3*$^{-/y}$ (dKO) mice at 4 weeks of age. Graphs represent percent spleen/body and liver/body weight of mice at 4 weeks of age (mean ± SD; n = 4; **p ≤ 0.01 by Student's t test).

(C) Flow cytometry analysis showing significant decreases in the Mac-1^{+} CD11c^{+} Ly-6G^{mid} histiocyte population but significant rescue of the Mac-1^{+} Ly-6G^{hi} mature neutrophil

population in BM cells of *Flcn*$^{f/f}$;*Vav-iCre*$^{Tg/+}$;*Tfe3*$^{-/y}$ (dKO) compared to *Flcn*$^{f/f}$;*Vav-iCre*$^{Tg/+}$ (*Flcn*-KO) mice at 4 weeks of age. The numbers in plots represent percentage of the gated population. Graphs represent percentage of the indicated population (mean ± SD; n = 4**p ≤ 0.01 by Student's t test).

(D) Graph represents percentages of hemophagocytes in BM cells from indicated mice (mean ± SD; n = 4; **p ≤ 0.01 by Student's t test; nd, not detected).

(E) Western blot showing expression of TFE3, LAMP1, and α-TUBULIN in BM cells from indicated mice.

(F) Quantitative RT-PCR analysis of expression of lysosomal genes in BM cells from indicated mice at 4 weeks of age. Data are normalized to *Actb*. Bars represent fold-change in values relative to control mice (mean ± SD; n = 4; *p ≤ 0.05, **p ≤ 0.01 by Student's t test).

(G) Quantitative RT-PCR showing expression of the gluconeogenesis genes *Fbp1* and *G6pc* in BM cells of indicated mice at 4 weeks of age. Data are normalized to *Actb*. Bars represent fold-change in values relative to control mice (mean ± SD; n = 4; *p ≤ 0.05, **p ≤ 0.01 by Student's t test; nd, not detected).

(H) Glycogen levels in spleen tissues from *Flcn*$^{f/f}$ (WT), *Tfe3*$^{-/y}$ (*Tfe3*-KO), *Flcn*$^{f/f}$;*Vav-iCre*$^{Tg/+}$ (*Flcn*-KO), and *Flcn*$^{f/f}$;*Vav-iCre*$^{Tg/+}$;*Tfe3*$^{-/y}$ (dKO) mice at 4 weeks of age, as determined using an enzyme-based fluorometric assay kit (mean ± SD; n = 4; **p ≤ 0.01 by Student's t test).

(I) Expression of the glycogenesis genes *Gys1*, *Gyg*1, and *Ppp1r3b* in spleen cells from *Flcn*$^{f/f}$ (WT), *Tfe3*$^{-/y}$ (*Tfe3*-KO), *Flcn*$^{f/f}$;*Vav-iCre*$^{Tg/+}$ (*Flcn*-KO), and *Flcn*$^{f/f}$;*Vav-iCre*$^{Tg/+}$;*Tfe3*$^{-/y}$ (dKO) mice at 4 weeks of age, as determined by quantitative RT-PCR. Data were normalized to *Actb* (mean ± SD; n = 4; *p ≤ 0.05, **p ≤ 0.01 by Student's t test).

(J) Western blot showing expression of GYG, GYS1, FBP1, and α-TUBULIN in spleen cells from indicated mice.

(K) ChIP-qPCR analysis of levels of TFE3 at TSSs of *Gys1* and *Gyg* in BM cells from *Flcn*$^{f/f}$ (WT), *Tfe3*$^{-/y}$ (*Tfe3*-KO), *Flcn*$^{f/f}$;*Vav-iCre*$^{Tg/+}$ (*Flcn*-KO), or *Flcn*$^{f/f}$;*Vav-iCre*$^{Tg/+}$;*Tfe3*$^{-/y}$ (dKO) mice. Relative amounts of ChIPed DNA are depicted as a percentage of input DNA (mean ± SD; n = 4; **p ≤ 0.01 by Student's t test).

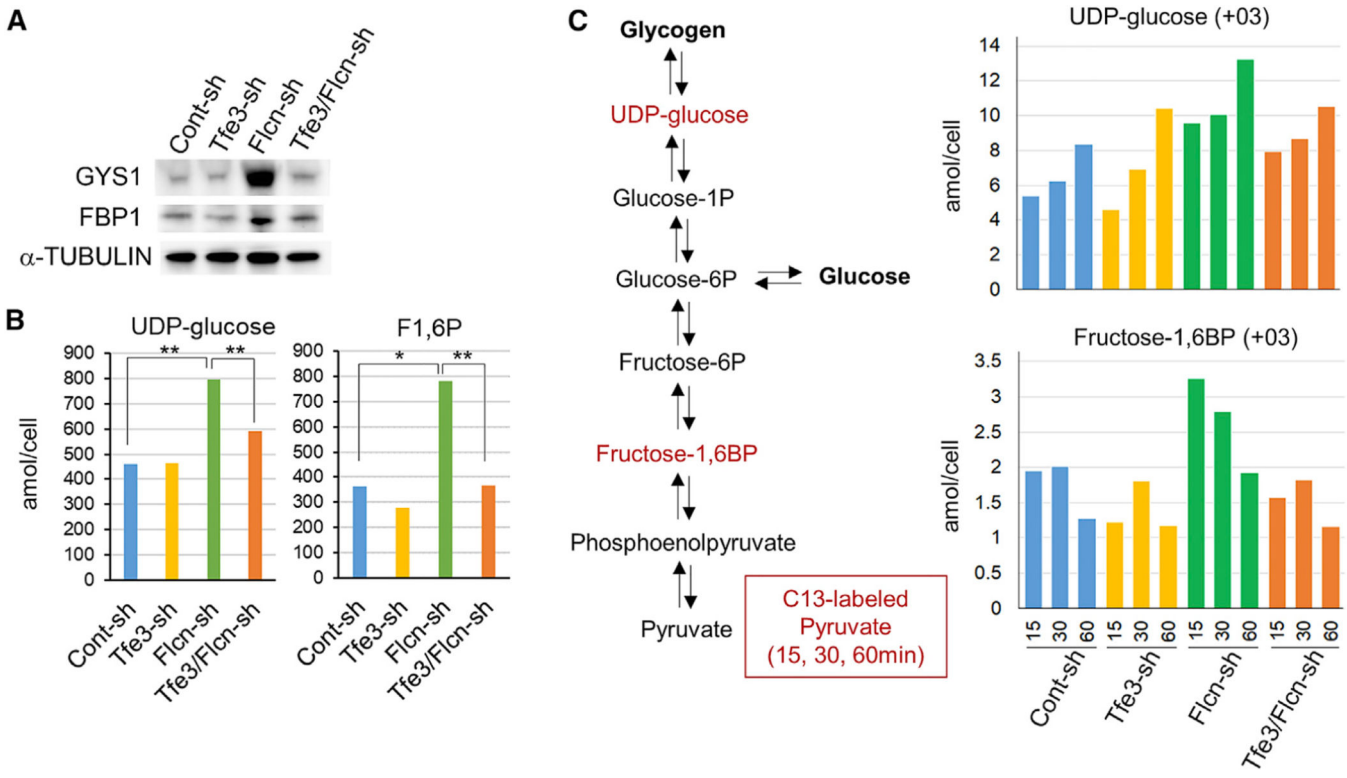

Figure 7. *Flcn* Loss Stimulates Glycogenesis Flux via *Tfe3*

(A) Western blot showing expression of GYS1, FBP1, and α-TUBULIN in RAW cells expressing indicated shRNA.

(B) The amount of UDP-glucose and fructose 1,6-bisphosphate (fructose-1,6BP) in RAW cells expressing indicated shRNA, as determined by CE-TOF/MS analysis. y axis represents mean amol/cell (n = 4; *p ≤ 0.05, **p ≤ 0.01 by unpaired t test).

(C) Schematic of gluconeogenesis and glycogenesis pathways from pyruvate. The amount of ^{13}C-labeled UDP-glucose and fructose-1,6BP in RAW cells expressing indicated shRNA after incubation with ^{13}C-fully labeled pyruvate for 15, 30, or 60 min, as determined by CE-TOF/MS analysis. y axis represents amol/cell.

KEY RESOURCES TABLE

REAGENT or RESOURCE	SOURCE	IDENTIFIER
Antibodies		
Rabbit polyclonal anti-TFE3	Sigma-Aldrich	Cat#HPA023881; RRID: AB_1857931
Rabbit monoclonal anti-LC3A/B (clone D3U4C)	Cell Signaling Technology	Cat#12741S; RRID: AB_2617131
Mouse monoclonal anti-GABARAP (clone 1F4)	MBL	Cat# M135–3; RRID: AB_10364779
Rabbit monoclonal anti-LAMP1 (clone C54H11)	Cell Signaling Technology	Cat#3243; RRID: AB_2134478
Mouse monoclonal anti-alpha-Tubulin (clone DM1A)	Sigma-Aldrich	Cat# T6199; RRID: AB_477583
Rabbit polyclonal anti-Trimethyl-Histone H3 Lysine 4 (H3K4me3)	Millipore	Cat#07–473; RRID: AB_1977252
Mouse monoclonal anti-RNA polymerase II CTD (clone 8WG16)	Millipore	Cat#05–952; RRID: AB_492629
Rabbit monoclonal anti-FBP1 (clone EPR4620)	Abcam	Cat#ab109732; RRID: AB_10864942
Rabbit monoclonal anti-Glycogen Synthase (clone 15B1)	Cell Signaling Technology	Cat#3886S; RRID: AB_2116392
Mouse monoclonal anti-GYG1 (clone 3B5)	Abnova	Cat#H00002992-M07; RRID: AB_530073
Anti-CD11c (HL3)-PE	BD Biosciences	Cat# 557401; RRID: AB_396684
Anti-Mac-1/CD11b (M1/70)-FITC	BioLegend	Cat#101206; RRID: AB_312789
Anti-Mac-1/CD11b (M1/70)-PE/Cy7	BioLegend	Cat#101216; RRID: AB_312799
Anti-Ly-6G (1A8)-APC	BioLegend	Cat#127614; RRID: AB_2227348
goat anti-rabbit IgG (H+L), Alexa Fluor 488	Thermo Fisher Scientific	Cat#A-11008; RRID: AB_143165
goat anti-mouse IgG (H+L), HRP	Bio-Rad	Cat#1706516; RRID: AB_11125547
goat anti-rabbit IgG (H+L), HRP	Bio-Rad	Cat#1706515; RRID: AB_11125142
Anti-Mouse c-kit/CD117 (2B8)-173Yb	Fluidigm	Cat#3173004B; RRID: AB_2811230
Anti-Mouse Mac-1/CD11b (M1/70)-172Yb	Fluidigm	Cat#3172012B; RRID: AB_2661809
Anti-Mouse Ly-6G/C/Gr-1 (RB6–8C5)-141Pr	Fluidigm	Cat#3141005B
Anti-Mouse anti-CD4 (RM4–5)-145Nd	Fluidigm	Cat#3145002B; RRID: AB_2687832
Anti-Mouse Sca-1/Ly-6A/E (D7)-169Tm	Fluidigm	Cat#3169015B; RRID: AB_2811233
Anti-Mouse CD48 (HM48–1)-154Sm	Fluidigm	Cat#3154004B; RRID: AB_2811232
Anti-Mouse CD150 (TC15)-167Er	Fluidigm	Cat#3167004B; RRID: AB_2811231
Anti-CD201 (clone eBio1560)-164Dy	eBioscience	Cat#16–2012-83; RRID: AB_657696
Anti-Mouse TER-119–162Dy	Fluidigm	Cat#3162003B
Anti-Mouse B220/CD45R (RA3–6B2)-160Gd	Fluidigm	Cat#3160012B
Anti-Mouse CD8a (53–6.7)-168Er	Fluidigm	Cat#3168003B; RRID: AB_2811241
Anti-Mouse NK1.1 (PK136)-170Er	Fluidigm	Cat#3170002B
Anti-pAkt [S473] (D9E)-152Sm	Fluidigm	Cat#3152005A; RRID: AB_2811246

REAGENT or RESOURCE	SOURCE	IDENTIFIER
Anti-pERK1/2 [T202/Y204] (D13.14.4E)-171Yb	DVS Sciences	Cat#3171010A; RRID: AB_2811250
Anti-pMAPKAPK2 [T334] (27B7)-159Tb	Fluidigm	Cat#3159010A; RRID: AB_2661828
Anti-beta-Catenin (D13A1)-165Ho	Fluidigm	Cat#3165027A; RRID: AB_2811247
Anti-p38 [T180/Y182] (D3F9)-156Gd	Fluidigm	Cat#3156002A; RRID: AB_2661826
Rabbit monoclonal anti-phospho-Jak2 [Tyr1008] (D4A8)-161Dy	Cell Signaling Technology	Cat#8082S; RRID: AB_10949104
Anti-pStat1 [Y701] (58D6)-153Eu	Fluidigm	Cat#3153003A; RRID: AB_2811248
Anti-pStat3 [Y705] (4/P-Stat3)-158Gd	Fluidigm	Cat#3158005A; RRID: AB_2811100
Anti-pStat5 [Y694] (47)-147Sm	Fluidigm	Cat#3147012A
Rabbit monoclonal anti-mTOR [phospho S2448] (EPR426(2)), 163Dy	Abcam	Cat#ab109268; RRID: AB_10888105
Rabbit monoclonal anti-phospho-AMPKα [Thr172] (40H9), 142Nd	Cell Signaling Technology	Cat#2535L; RRID: AB_331250
Rabbit polyclonal anti-HIF-1alpha-150Nd	Santa Cruz	Cat#sc-10790; RRID: AB_2116990
Purified Rat Anti-Mouse CD16/CD32 (Mouse BD Fc Block) Clone 2.4G2 (RUO)	BD Biosciences	Cat#553141; RRID: AB_394656
Chemicals, Peptides, and Recombinant Proteins		
Poly(I:C) HMW	InvivoGen	Cat#tlrl-pic; CAS: 31852–29-6
FuGENE 6 Transfection Reagent	Promega	Cat#E2691
ProLong Gold Antifade Mountant with DAPI	Thermo Fisher Scientific	Cat#P36941
pHrodo Red *E. coli* BioParticles Conjugate for Phagocytosis	Thermo Fisher Scientific	Cat#P35361
pHrodo Green *E. coli* BioParticles Conjugate for Phagocytosis	Thermo Fisher Scientific	Cat#P35366
pHrodo Red, succinimidyl ester (pHrodo Red, SE)	Thermo Fisher Scientific	Cat#P36600
LysoTracker Deep Red	Thermo Fisher Scientific	Cat#L12492
CellTrace CFSE Cell Proliferation Kit, for flow cytometry	Thermo Fisher Scientific	Cat#C34570
SODIUM PYRUVATE (3–13C, 99%)	Cambridge isotope laboratories	Cat#CLM-2440–0.5
Puromycin	InvivoGen	Cat#ant-pr-1; CAS: 58–58-2
Blasticidin	InvivoGen	Cat#ant-bl-05
Pierce Protein A/G Magnetic Beads	Thermo Fisher Scientific	Cat#88802
RIPA Lysis and Extraction Buffer	Thermo Fisher Scientific	Cat#89900
4X Laemmli sample buffer	Bio-Rad	Cat#1610747
PowerUp SYBR Green Master Mix	Thermo Fisher Scientific	Cat#A25742
Dexamethasone	Sigma-Aldrich	Cat#D1756; CAS: 50–02-2
TRIzol	Thermo Fisher Scientific	Cat#15596026
Critical Commercial Assays		
Glycogen Colorimetric/Fluorometric Assay Kit	BioVision	Cat#K646
PAS stain kit	MUTO PURE CHEMICALS	Cat#15792
SuperScript IV VILO Master Mix with ezDNase Enzyme	Thermo Fisher Scientific	Cat#11766050

REAGENT or RESOURCE	SOURCE	IDENTIFIER
Deposited Data		
Deposited dataset GSE75822: Tfe3 ChIP-seq in RAW 264.7 cells	Pastore et al., 2016	GEO: GSE75822
Experimental Models: Cell Lines		
Mouse: RAW 264.7	ATCC	ATCC TIB-71
Experimental Models: Organisms/Strains		
Mouse: *Flcn*$^{fl/fl}$	Masaya Baba Lab	N/A
Mouse: *Tfe3*$^{-/-}$	Lino Tessarollo Lab	N/A
Mouse: *Vav-iCre*	Jackson laboratory	008610
Mouse: *Mx1-Cre*	Jackson laboratory	003556
Oligonucleotides		
Primers for qPCR assays, see Table S1	This paper	N/A
shRNA targeting sequence: mFlcn: GCTTCAAGTCTCTTCGACACAT	Betschinger et al., 2013	N/A
shRNA targeting sequence: m*Tfe3*: GCCTAACATCAAACGCGAGAT	Betschinger et al., 2013	N/A
Recombinant DNA		
Plasmid: pMDLg/pRRE	Dull et al., 1998	Addgene Plasmid #12251
Plasmid: pRSV-Rev	Dull et al., 1998	Addgene Plasmid #12253
Plasmid: pMD2.G	Dull et al., 1998	Addgene Plasmid #12259
Plasmid: pLV[shRNA]-Puro-U6 > mFlcn[shRNA#6]	VectorBuilder	N/A
Plasmid: pLV[shRNA]-Bsd-U6 > mTfe3[shRNA#11]	VectorBuilder	N/A
Plasmid: pCAG-mTfe3.GR-IRES-Puro	Baba et al., 2018	N/A
Software and Algorithms		
FlowJo 10.1	Tree Star	N/A
QuantStudio Design and Analysis Software 1.3.1	Thermo Fisher Scientific	N/A
Image Lab 5.2.1	Bio-Rad	N/A
Integrative Genomics Viewer (IGV)	Broad Institute	N/A
GraphPad Prism 6/7	GraphPad	N/A
NIS-Elements	Nikon	N/A
Cytobank	Cytobank, Inc.	N/A